

2015-01-01

# Mechanical and Optical Characterization of Tungsten Oxynitride (W-O-N) Nano-Coatings

Oscar Roberto Nunez

University of Texas at El Paso, ornunez@miners.utep.edu

Follow this and additional works at: [https://digitalcommons.utep.edu/open\\_etd](https://digitalcommons.utep.edu/open_etd)



Part of the [Nanoscience and Nanotechnology Commons](#)

---

## Recommended Citation

Nunez, Oscar Roberto, "Mechanical and Optical Characterization of Tungsten Oxynitride (W-O-N) Nano-Coatings" (2015). *Open Access Theses & Dissertations*. 915.

[https://digitalcommons.utep.edu/open\\_etd/915](https://digitalcommons.utep.edu/open_etd/915)

This is brought to you for free and open access by DigitalCommons@UTEP. It has been accepted for inclusion in Open Access Theses & Dissertations by an authorized administrator of DigitalCommons@UTEP. For more information, please contact [lweber@utep.edu](mailto:lweber@utep.edu).

MECHANICAL AND OPTICAL CHARACTERIZATION OF TUNGSTEN  
OXYNITRIDE (W-O-N) NANO-COATINGS

OSCAR ROBERTO NUNEZ

Department of Mechanical Engineering

APPROVED:

---

Ramana Chintalapalle, Ph.D., Chair

---

Calvin Stewart, Ph.D.

---

David Roberson, Ph.D.

---

Charles Ambler, Ph.D.  
Dean of the Graduate School

Copyright ©

by

Oscar Roberto Nunez

2015

## **Dedication**

Dedicated to my supportive parents, whom without, this work would not have been possible.

MECHANICAL AND OPTICAL CHARACTERIZATION OF TUNGSTEN  
OXYNITRIDE NANO-COATINGS

by

OSCAR ROBERTO NUNEZ, B.S.

THESIS

Presented to the Faculty of the Graduate School of

The University of Texas at El Paso

in Partial Fulfillment

of the Requirements

for the Degree of

MASTER OF SCIENCE

Department of Mechanical Engineering

THE UNIVERSITY OF TEXAS AT EL PASO

December 2015

## Acknowledgements

I would like to first and foremost, thank my advisor Dr. Ramana Chintalapalle for believing in me and my abilities. I am especially appreciative of his dedication to my advancement as an engineer and researcher, and for offering me additional research opportunities outside of the university. The rich experience gained through the internships, this thesis work in the laboratory, and his mentorship added extra confidence and belief in my abilities and credentials as an engineer. I am very thankful that I was able to participate in a novel area of research, with the guidance that I received all along the way.

I would also like to thank Dr. Calvin Stewart and Dr. David Roberson for being on my thesis committee. Their valuable feedback of my work has been much appreciated.

I am grateful for all of the support that I received from my research team members Adbeel, Gustavo, Mirella, Ernesto, Satya, Diego and Gabriel, without whom this work would not have been possible.

I am also appreciative of all of my friends and loved ones for their support of me, during my time at UTEP and while completing my M.S.

I would like to acknowledge UTEP's "***Graduate Bridge Program for Highly Achieving Engineering and Computer Science Students***" for their financial support throughout graduate school. My advisor and I also acknowledge with pleasure, support from the National Science Foundation (NSF) with NSF-PREM grant # DMR-1205302. However, any opinions, findings, and conclusions or recommendations expressed in this material are those of the author(s) and do not necessarily reflect the views of the National Science Foundation.

## Abstract

Aation and cation doping of transition metal oxides has recently gained attention as a viable option to design materials for application in solar energy conversion, photo-catalysis, transparent electrodes, photo-electrochemical cells, electrochromics and flat panel displays in optoelectronics. Specifically, nitrogen doped tungsten oxide ( $\text{WO}_3$ ) has gained much attention for its ability to facilitate optical property tuning while also demonstrating enhanced photo-catalytic and photochemical properties. The effect of nitrogen chemistry and mechanics on the optical and mechanical properties of tungsten oxynitride (W-O-N) nano-coatings is studied in detail in this work. The W-O-N coatings were deposited by direct current (DC) sputtering to a thickness of  $\sim 100$  nm and the structural, compositional, optical and mechanical properties were characterized in order to gain a deeper understanding of the effects of nitrogen incorporation and chemical composition. All the W-O-N coatings fabricated under variable nitrogen gas flow rate were amorphous. X-ray photoelectron spectroscopy (XPS) and Rutherford backscattering spectrometry (RBS) measurements revealed that nitrogen incorporation is effective only for a nitrogen gas flow rates  $\geq 9$  sccm. Optical characterization using ultraviolet-visible-near infrared (UV-VIS-NIR) spectroscopy and spectroscopic ellipsometry (SE) indicate that the nitrogen incorporation induced effects on the optical parameters is significant. The band gap ( $E_g$ ) values decreased from  $\sim 2.99$  eV to  $\sim 1.89$  eV indicating a transition from insulating  $\text{WO}_3$  to metallic-like W-N phase. Nano-mechanical characterization using indentation revealed a corresponding change in mechanical properties; maximum values of 4.46 GPa and 98.5 GPa were noted for hardness and Young's modulus, respectively. The results demonstrate a clear relationship between the mechanical, physical and optical properties of amorphous W-O-N nano-coatings. The correlation presented in this thesis could provide a road-map to optimize and produce W-O-N nano-coatings with desired optical and mechanical properties for a given technological application in the field where structure, mechanical and optical properties are important.

## Table of Contents

Acknowledgements.....	v
Abstract.....	vi
Table of Contents.....	vii
List of Tables .....	ix
List of Figures .....	x
Chapter 1: Introduction .....	1
1.1 Tungsten Oxides .....	2
1.1.1 Chromogenic Devices.....	2
1.1.2 Photo-electrochemical Applications of WO <sub>3</sub> .....	3
1.2 Tungsten Nitrides.....	4
1.2.1 Diffusion Barriers .....	4
1.2.2 Gate Electrodes .....	6
1.2.3 Hard Coatings .....	7
1.3 Tungsten Oxynitrides.....	7
1.3.1 Structure and Surface Morphology.....	8
1.3.2 Chemical Composition.....	10
1.3.3 Electro-Optical Properties.....	11
1.3.4 Electro-Optical Properties of Similar Metal Oxynitrides .....	13
1.3.5 Mechanical Properties.....	14
1.3.6 Mechanical Properties of Zirconium Tungsten Nitrides.....	17
Chapter 2: Literature Review.....	19
2.1 Works Published on Tungsten Oxynitrides .....	19
2.1.1 Electro-Optical Properties.....	19
2.1.2 Mechanical Properties.....	20
2.2 Goals and Objectives of Present Work .....	21
Chapter 3: Methodology .....	24
3.1 DC Sputtering Deposition.....	24
3.2 Characterization Methods .....	24

3.2.1 X-Ray Diffraction .....	24
3.2.2 X-Ray Photoelectron Spectroscopy .....	25
3.2.3 Rutherford Backscattering Spectrometry .....	26
3.2.4 UV-VIS-NIR Spectroscopy .....	27
3.2.5 Ellipsometry .....	28
3.2.6 Nano-Indentation .....	28
3.3 Deposition .....	30
Chapter 4: Results and Discussion .....	32
4.1 Structural Properties .....	32
4.2 Chemical Composition .....	33
4.3 Optical Properties .....	37
4.4 Modeling The Optical Data .....	46
4.5 Mechanical Properties .....	53
Chapter 5: Physical, Mechanical, Chemical and Optical Property Correlation .....	57
Chapter 6: Conclusions .....	65
Chapter 7: Future Work .....	67
References .....	68
Vita .....	74

## List of Tables

Table 3.1. Sputtering conditions employed for the deposition of W-O-N nano-coatings. ....	31
Table 4.1: Chemical composition of W-O-N nano-coatings as calculated by SIMNRA from the RBS spectra as a function of nitrogen flow .....	37
Table 4.2: Tauc-Lorentz oscillator parameters used to fit the optical constants for W-O-N nano-coatings as a function of nitrogen flow rate.....	42
Table 4.3: Calculated values for $E_g$ , $E_0$ and $E_d$ as gathered by the single-oscillator method for fitting the index of refraction ( $n$ ) .....	49
Table 4.4: The results of the complete analysis of the fitting of the refractive index ( $n$ ) to the single-oscillator model taking into account the chemical composition of the nano-coatings .....	51

## List of Figures

Figure 1.1: Schematic for an electrochromic device indicating the movement of ions through a layer of an electrochromic film, altering the film's optical properties [1].....	3
Figure 1.2: Schematic of experiments done by Uekubo et al. describing the performance of different phases of tungsten nitride against copper diffusion and reaction with the substrate [17] .....	5
Figure 1.3: Schematic of basic metal-oxide capacitor for use in semiconductor devices .....	6
Figure 1.4: SEM image of (a) undoped and (b) nitrogen doped WO <sub>3</sub> coatings showing decreased grain size [3] .....	9
Figure 1.5: Optical constants $n$ and $k$ as it relates to increasing oxygen flow [46] .....	12
Figure 1.6: Band gap values as it relates to the normalized nitrogen partial pressure [43] .....	13
Figure 1.7: $ah\nu$ vs. $h\nu$ curve of Ti-O-N exemplifying two linear regions [59].....	14
Figure 1.8: Parreira et al. show a correlation between the hardness and residual stress [51] .....	15
Figure 1.9: Mechanical properties of Zr-W-N at FCC, amorphous then FCC + HCP structures [60].....	17
Figure 3.1: Schematic of RBS experimental setup [64] .....	27
Figure 3.2: Typical Load vs. Displacement graph [68] .....	29
Figure 4.1: GIXRD patterns of W-O-N nano-coatings deposited at various nitrogen gas flow rates. The amorphous nature of the W-O-N coatings is evident from the patterns. ....	33
Figure 4.2: XPS survey spectrum of W-O-N nano-coatings deposited with 9 sccm of nitrogen flow .....	34
Figure 4.3: N 1s peak evolution as a function of nitrogen gas flow rate (a) and the area of the N 1s peak obtained via peak fitting of the high resolution XPS spectra (b).....	35
Figure 4.4: RBS spectra of W-O-N nano-coatings with both experimental and simulated (SIMNRA) data shown for the samples of pure WO <sub>3</sub> deposited with no nitrogen (a) and W-O-N deposited with 9 sccm of nitrogen flow (b) .....	36
Figure 4.5: Optical spectral transmittance curves at various nitrogen flow rates. A shift in absorption can be seen with increasing nitrogen flow rate and is indicated by the arrow.....	38
Figure 4.6: Optical stack model of W-O-N nano-coatings used for ellipsometry data analysis...	39
Figure 4.7: Spectral dependence of $\psi$ and $\Delta$ for W-O-N nano-coatings grown with varying nitrogen flow with experiment data and modeling curves shown. ....	41
Figure 4.8: Band gap variation in W-O-N nano-coatings with varying nitrogen flow rate. The variation of $E_g$ indicates a change in the electronic structure of the coatings as nitrogen is incorporated. ....	42
Figure 4.9: Refractive Index ( $n$ ) and Extinction Coefficient ( $k$ ) values at 550 and 632 nm, displayed as a function nitrogen flow .....	44
Figure 4.10: The dispersion profiles of index of refraction ( $n$ ) of W-O-N nano-coatings with little or no nitrogen incorporation (a) and increasing nitrogen incorporation (b) .....	45
Figure 4.11: $k(\lambda)$ curves of W-O-N nano-coatings with little or no nitrogen incorporation (a) and increasing nitrogen incorporation (b).....	46
Figure 4.12: Singular $(n^2-1)-I$ vs. $E^2$ plot, at 9 sccm nitrogen flow rate, fitted using a linear expression. In order to approximate the band gap using this method $E_0$ and $E_d$ must be calculated by setting $E_0/E_d$ equal to the y-intercept and $-(E_0E_d)^{-1}$ equal to the slope.....	47
Figure 4.13: $(n^2-1)^{-1}$ vs. $E^2$ plots for the index of refractive ( $n$ ) fitted using the single-oscillator model.....	48

Figure 4.14: $E_0$ and $E_d$ , as calculated by fitting the index of refraction ( $n$ ) to the single-oscillator model, and as a function of the flow rate of nitrogen gas .....	49
Figure 4.15: $Z_a$ and $N_e$ as calculated using the chemical composition of the W-O-N nano-coatings as calculated by RBS analysis.....	50
Figure 4.16: $(\alpha h\nu)^{1/2}$ vs. $h\nu$ plot for W-O-N nano-coatings deposited with 15 sccm of nitrogen. The linear region of the plot is extrapolated to $h\nu = 0$ in order to calculate the value for $E_g$ .....	52
Figure 4.17: $(\alpha h\nu)^{1/2}$ vs. $h\nu$ plot for various W-O-N thin nano-coatings deposited increasing nitrogen gas flow rates .....	52
Figure 4.18: Optical band gap ( $E_g$ ) values as a function of nitrogen flow rate as determined by applying the Single-Oscillator model and Tauc Relation to the optical constants found by SE ..	53
Figure 4.19: Mechanical properties, hardness and Young's modulus, of W-O-N nano-coatings represented as a function of nitrogen gas flow rate and measured by nano-indentation tests. ....	55
Figure 4.20: Density variation of W-O-N nano-coatings with nitrogen flow rate. It is evident that the coating's density increases with increasing nitrogen gas flow rate. ....	56
Figure 5.1: Proposed electronic structure model to account for the observed changes in the band gap of W-O-N nano-coatings. The variable, lower band gap in W-O-N corresponds to the electronic transitions from the new valence band, which is formed by a mixture of O 2p and N 2p states.....	59
Figure 5.2: The hardness, cation coordination number ( $N_c$ ) and density of W-O-N coatings as a function of nitrogen flow rate. A direct relation between the mechanical properties (hardness) and physical properties ( $N_c$ and Density) determined from optical properties is apparent in this comparison.....	62
Figure 5.3: Density variation of W-O-N nano-coatings with nitrogen flow rate. It is evident that the coating's density increases with increasing nitrogen gas flow rate. ....	63
Figure 5.4: Proposed correlation between physical properties (density), chemistry (composition), and electronic structure (optical properties) of W-O-N nano-coatings. ....	64

## Chapter 1: Introduction

Today's need to minimize the carbon footprint left behind by all traditional energy and chemical industries require designing and realizing materials that can facilitate the production of clean energy and the maintaining of high efficiency in extreme environments. In this regard, researchers are constantly searching for novel strategies and designing new materials for functional applications. Currently, oxynitride thin films and coatings are of particular interest in view of their ability to combine the traditional electro-optical properties of oxides with the mechanical properties of nitrides. When a metal is reacted in oxygen and nitrogen, the resulting material can exhibit a combination of mechanical and optical properties in addition to oxidation resistance and structural stability at elevated temperatures.

Tungsten oxide ( $\text{WO}_3$ ) is a semiconducting material; it well known for chromogenic properties and optical properties that allow for its ability to utilize a wide portion of the solar spectrum [1-10]. These properties have allowed for  $\text{WO}_3$  to be applied in electrochromic films for energy efficient windows, display devices and as photoelectrochemical cells (PEC) for hydrogen production, photocatalysis and solar cells [1-20]. Similarly, for decades, tungsten nitrides have had a vital role in microelectronics as diffusion barriers, gate electrodes and other components as well as in industrial applications as hard coatings. By incorporating nitrogen into  $\text{WO}_3$ , thus producing tungsten oxynitride (W-O-N) nano-coatings, it is possible to tune the desired optical and mechanical properties based on chemical composition. This is the impetus for this study, which will provide an overview of how the nitrogen content and overall chemical composition influences the optical and mechanical properties of tungsten oxynitride nano-coatings, accomplishing the desired optical property tuning combined with the traditionally advantageous characteristics of nitrides with oxidation resistance and structural stability at elevated temperatures. Some general introduction to the specific materials and topics relevant to this thesis work is presented in the following sections.

## 1.1 TUNGSTEN OXIDES

Tungsten oxide ( $\text{WO}_3$ ) and  $\text{WO}_3$ -based complex oxide materials have been used in many industries for their highly attractive electro-optical, structural, and electronic properties and for their use as a chromogenic material [1-10]. Based on a modified rhenium oxide ( $\text{ReO}_3$ ) structure,  $\text{WO}_3$  phase transitions are highly dependent upon temperature; the sequence follows from a low temperature monoclinic structure,  $\epsilon$ - $\text{WO}_3$  below 230 °K, to a triclinic,  $\delta$ - $\text{WO}_3$  from 230-300 °K, room temperature monoclinic,  $\gamma$ - $\text{WO}_3$  from 300-600 °K, orthorhombic,  $\beta$ - $\text{WO}_3$  from 600-1020 °K, and a tetragonal structure,  $\alpha$ - $\text{WO}_3$  above 1170 °K [11-13].  $\text{WO}_3$  thin films and nanostructures exhibit an optical band gap of  $\sim 2.4\text{-}3.2$  eV, as well as absorption extending from the blue part of the visible region to the ultraviolet region and high transmission in the near-infrared (IR) to visible spectrum [5-7]. Tungsten oxide's properties allow for good accommodation of oxidation state alterations by field-aided ion intercalation and for proper band alignment for solar cell applications [4-5]. Below is a brief explanation of how these properties can be directly applied to different device designs.

### 1.1.1 Chromogenic Devices

Due to tungsten oxide's "electrically controllable" optical properties their use in chromogenic applications, such as energy efficient windows and display devices, has been extensively explored in literature. Granqvist et al. described that by inserting or extracting ions from an electrochromic film, the optical properties can be modified; as electrons enter in conjunction with ions to obtain charge neutrality. A schematic of such a device is shown in Figure 1.1 [1]. A voltage is applied to two transparent conductors that surround a transparent conductor and electrochromic films that lay on either side of an ion conductor. Ions are then inserted or extracted from the electrochromic film, resulting in a change in color. Studies of electrochromic thin films attempt to describe the mechanisms of accomplishing a change in oxidation state and the promotion of reversible spectral absorption properties [1-4]. Further

improvements to the electrochromic performance of  $\text{WO}_3$  films and coatings are made with the addition of a dopant, usually Ti [6, 9].

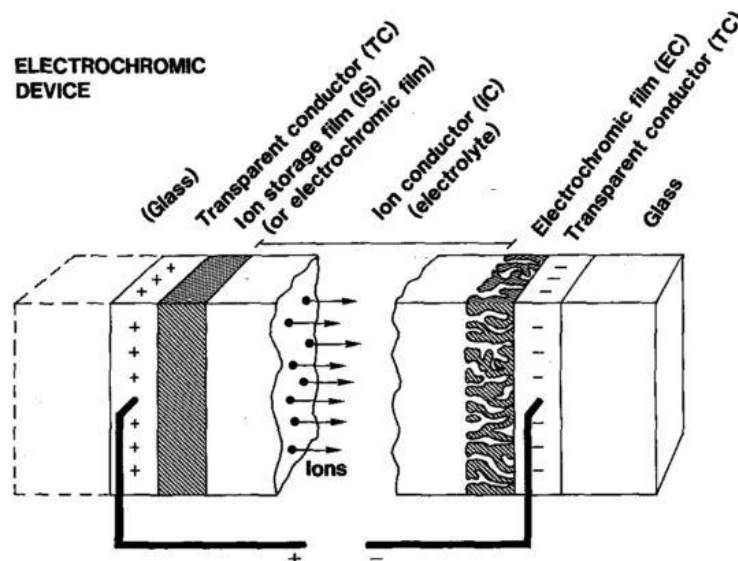


Figure 1.1: Schematic for an electrochromic device indicating the movement of ions through a layer of an electrochromic film, altering the film's optical properties [1]

### 1.1.2 Photo-electrochemical Applications of $\text{WO}_3$

$\text{WO}_3$  thin films have also been used as electrodes in photoelectrochemical cells (PEC), transparent back contacts for solar cell designs and oxidation resistive gas sensors [5-8]. PEC technology alone has a range of applications such as use in hydrogen production, photocatalysis and solar cells. An example of PEC technology being applied is presented by Higashimoto et al in which the author forms a  $\text{WO}_3/\text{TiO}_2$  hybrid material that uses photoelectrochemical conversion of solar energy in order to obtain photo-induced charge separation [8]. PEC technology can also take advantage of photocatalytic properties and induce water-splitting by taking advantage of the photo-induced electron and hole formation, resulting in the formation of hydrogen. Other applications for tungsten oxide are as transparent back contacts for different solar cell designs as well as other applications taking advantage of the material's physical properties [5]. Another huge advantage of  $\text{WO}_3$  is its resistivity to oxidation which eventually led to their use in gas sensors and as a result has been studied further for their mechanical

properties as an alternative to tungsten nitride hard coatings for highly corrosive environments [8-10].

## **1.2 TUNGSTEN NITRIDES**

Tungsten nitride coatings are traditionally studied for use as diffusion barriers in microelectronics [17-24], gate electrodes in semiconductor devices [25-30], hard coatings to protect from mechanical wear [16, 31-35] or as Schottky Contacts [25, 36]. Several studies conducted by Shen et al. aim to grasp the full knowledge of the relationship between different parameters such as the deposition condition have on the internal stress, microstructure, elemental concentration [37-39]. More recently studies have attempted to fine tune properties by changing the substrate bias voltage, deposition methods or adding tungsten oxide layers [40-42]. Below is a more detailed review of the early applications of tungsten nitride coatings to further understand the importance of studying these coatings for further application in advanced technology.

### **1.2.1 Diffusion Barriers**

Tungsten nitride's use as a diffusion barrier has been well documented and developed for the past few decades. For use in increasingly smaller semiconductor devices, diffusion barriers have been manufactured to improve the performance of semiconductor contacts. Diffusion barriers lay between the contact materials, usually copper or aluminum, and the silicon substrate in order to prevent diffusion and any reaction between the material and the substrate. Uekubo et al. have reported that without the use of diffusion barriers, copper contacts diffuse rapidly into silicon substrates, causing the formation of copper silicide which can be visualized in Figure 1.2 [17]. This formation creates a time delay and Joule heat generation detrimental to performance of semiconductor contacts [17].

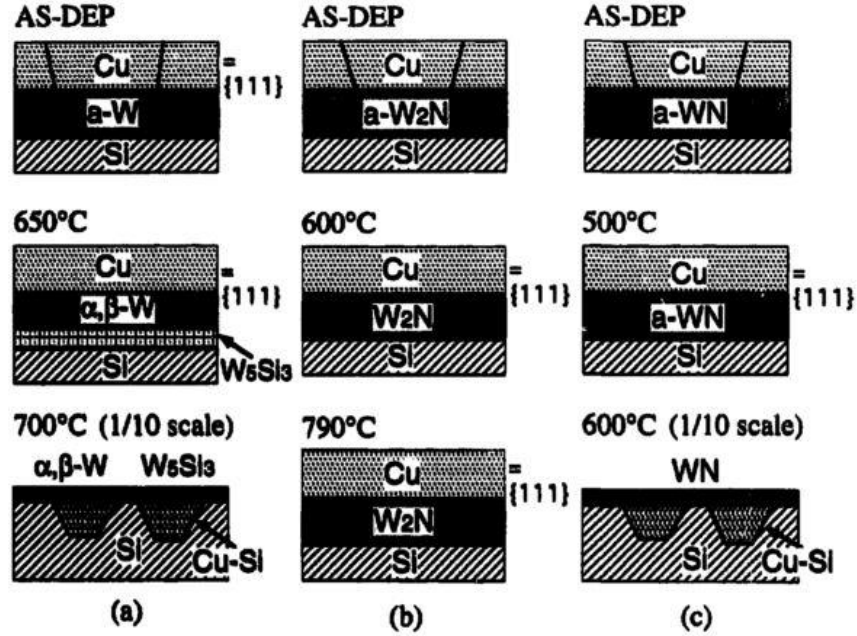


Figure 1.2: Schematic of experiments done by Uekubo et al. describing the performance of different phases of tungsten nitride against copper diffusion and reaction with the substrate [17]

An early study of tungsten nitride by Kattelus et al. as diffusion barrier reported that ideally the material would be chemically and mechanically stable, as well as electronically conductive, while inhibiting inter-diffusion of the contact material into the substrate [18]. Traditionally nitrogen incorporation into the diffusion barrier material is said to introduce impurities that are implanted into grain boundaries to counteract diffusion [18]. Many of the subsequent studies have concentrated on improving thermal stability and overall performance by investigating how the structure and the addition of Al over-layers could alter results [18-20].

The next development in diffusion barriers was a change in contact material from aluminum to copper. Results published in the literature demonstrated that tungsten nitride remained stable up to 750 °C and coatings with a  $W_2N$  phase demonstrated the best properties and performance [17, 21-22]. Some authors also focused on improving diffusion barrier properties further by employing chemical vapor deposition (CVD) methods rather than physical

vapor deposition (PVD) used in past articles, arguing reactive sputtering resulted in inadequate step coverage of the coating [23-24].

### 1.2.2 Gate Electrodes

Tungsten nitride coatings were also used as gate electrodes in metal-oxide semiconductor devices [26]. Specifically the coatings are used as gate electrodes in capacitors, as seen in the Figure 1.3, which can then be used in devices such as transistors. The purpose of the gate material is to regulate the voltage supplied to the capacitor since traditional polycrystalline silicon gate electrodes suffer from high resistance, gate depletion and boron penetration from the gate material to the channel region [29-30]. Depositing the gate material without damaging the dielectric material underneath is a challenge; the employment of wet hydrogen heat treatment is used as a remedy to re-oxidize the dielectric material without oxidizing the gate electrode [27]. In response, Moriwaka et al. attempted to improve the gate dielectric reliability by using reactive sputtering to deposit the tungsten nitride gate electrode [27].

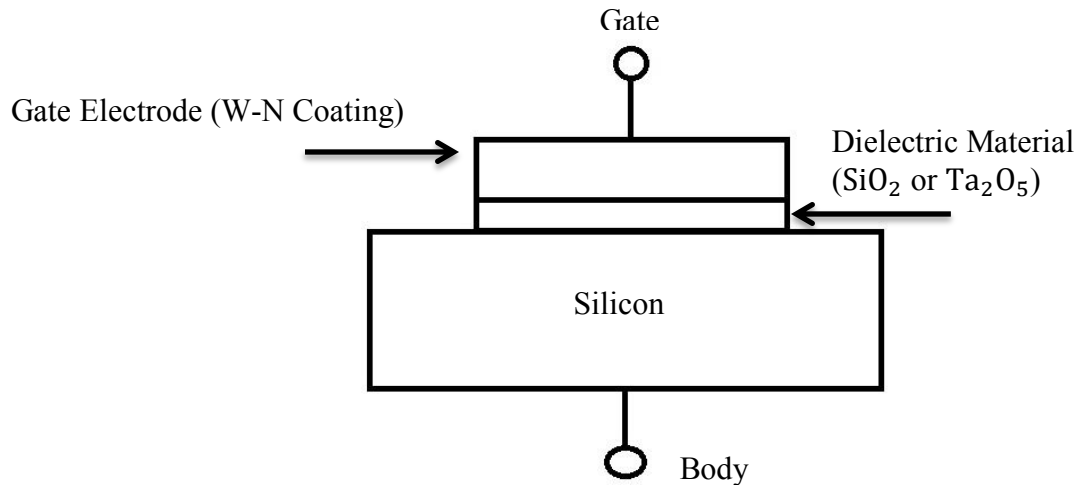


Figure 1.3: Schematic of basic metal-oxide capacitor for use in semiconductor devices

The next improvement for such devices came in altering the crystal phase, grain size and dielectric material from  $\text{SiO}_2$  to  $\text{Ta}_2\text{O}_5$  due to higher dielectric constant ( $k$ ) values [28-30]. As

stated by Jiang et al., it was found that tungsten nitride exhibits lower leakage current than titanium nitride at elevated temperature leading to their study of the material after post-annealing treatment [29].

### **1.2.3 Hard Coatings**

Tungsten nitrides are traditionally known as wear resistant hard coatings since they exhibit high melting point, low friction coefficient and extreme hardness [31]. Hardness of thin coatings range from 28-40 GPa, results were best when a hexagonal WN phase was observed and reactive sputtering was used to fabricate the coatings [31-33]. Polcar et al. studied the effect of high temperature annealing on the mechanical and wear resistance properties of tungsten nitride and found that hardness of the coatings decreased with annealing temperature and that annealing over 300 °C is detrimental to wear resistance [34]. Interestingly, a separate study also conducted by Polcar et al. revealed the friction coefficient of tungsten oxide coatings were better than those exhibited in tungsten nitrides [16]. Consequently, those studying tungsten nitrides for application as hard coatings attempt to optimize deposition parameters so that the correct composition, phases, microstructure and adhesion exist so that the best wear resistance and hardness values are accomplished [35].

## **1.3 TUNGSTEN OXYNITRIDES**

Tungsten oxynitrides essentially combine all of the favorable properties of both tungsten oxides and nitrides, when its composition is optimized. The available publications on W-O-N thin films and coatings concentrate on structural effects to the electric, optical and electrochromic properties [3, 6, 43-48]. Thus far however, there have not been many experiments to determine the comprehensive optical, physical, chemical and mechanical behavior correlation in tungsten oxynitrides. From mechanical point of view, only a few selected attempts were made to probe hardness and Young's modulus values of W-O-N nano-coatings [49-53]. This section serves as a summary of the properties of tungsten oxynitride thin films and coatings, and similar materials as found in the literature.

### 1.3.1 Structure and Surface Morphology

Several studies on the growth of tungsten oxynitride films and coatings are available with results displaying structural characteristics as dependent on dopant incorporation. Most of the studies agree that the growth of the coatings results in an amorphous structure unless there is a significant amount of nitrogen introduced into the system, partial pressure rates greater than .922 [3, 43-44, 46, 49-51]. However, when a sufficient amount of nitrogen is incorporated into the coating,  $W_2N$  phases appear in the form of (111) and (200) peaks usually centered near  $2\theta = 37^\circ$  and  $43^\circ$  respectively [3, 49-50] with an additional peak (220) also associated with the  $W_2N$  phase, near  $2\theta = 63^\circ$  [43, 53]. These peaks indicate a  $W_2N$  face-centered cubic structure [53].

Several authors investigated the structure of the coatings further by studying the surface morphology of the samples using; atomic force microscopy (AFM), transmission electron microscopy (TEM) and/or scanning electron microscopy (SEM). Grains of different sizes, depending on the amount of nitrogen incorporation, were observed in samples regardless of a crystalline structure existing. Khamseh reported a worm like structures in tungsten nitride coatings and a pebble like structure in amorphous tungsten oxynitride, while Sun et al. found randomly distributed grains with pores between them [47, 53]. The other observation was the reduction in the grain size (Figure 1.4) when nitrogen incorporation is increased [3, 10, 47]. However Shen et al. reports a finer structure as oxygen partial pressure increases, but this is attributed to an increase in impurities and a sign of an amorphous alloy [50].

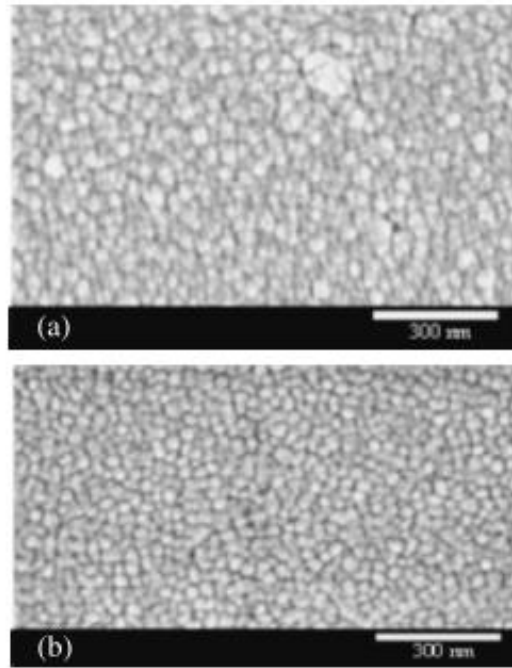


Figure 1.4: SEM image of (a) undoped and (b) nitrogen doped  $\text{WO}_3$  coatings showing decreased grain size [3]

Thermal annealing has been considered by several research groups to form a well-ordered structure from amorphous structure, which was a result of nitrogen incorporation. After annealing amorphous samples to a temperature of 650 °C, for 30 minutes, a single phase  $\text{W}_2\text{N}$  structure begins to form [49]. As the annealing temperature was raised, the  $\text{W}_2\text{N}$  structure remains stable up until at least 800 °C [52] and even up to 900 °C [49]; higher than the 800° possible with a tungsten nitride coating [49]. This is attributed to the formation of a thin oxide layer, on the surface of the coating, which stabilizes the  $\text{W}_2\text{N}$  structure of the coating during exposure to high temperatures by preventing nitrogen escaping through the surface during the annealing process [49-50, 52]. Evidence of the tungsten oxide layer was found in XRD studies [49, 52]. The thin layer of tungsten oxide on the surface also results in a change in mechanical properties which is discussed in the subsequent sections.

### 1.3.2 Chemical Composition

Chemical composition usually will have a profound influence on the characteristics of tungsten oxynitride films and coatings. Therefore, composition of the W-O-N coatings is usually the first thing considered before attempting to study their properties. Though various methods were used to find the composition of the coatings (RBS, XPS, EPMA and EDAX), results were fairly consistent. Several authors showed that with an increase of oxygen flow or partial pressure during deposition, there is a steady increase in oxygen concentration and a decrease in tungsten and nitrogen concentrations [46, 50, 53]. This is because tungsten has a higher attraction to oxygen than it does to nitrogen [43, 46, 51]. Mohammed et al. explained that thermodynamically “the heat of formations for  $\text{WO}_3$  and  $\text{WO}_2$  are -842.9 kJ/mol and -589.7 kJ/mol, respectfully”, while for  $\text{W}_2\text{N}$  and  $\text{WN}$  are -22 kJ/mol and -15 kJ/mol respectively, showing that the formation of W-O is preferred over that of W-N [43]. Louro et al. goes a step further and shows experimentally that when the partial pressure of both nitrogen and oxygen were identical during deposition that the concentration of oxygen was higher than that of nitrogen within the coating [52].

Notably no significant nitrogen incorporation takes place unless an extremely high amount of nitrogen, for example a partial pressure of 0.742 or 0.840, is present during deposition [43-44]. The composition and structure of the coatings were affected by the fact that tungsten form chemical bonds more easily with oxygen than it does with nitrogen, as well as inefficient substrate temperature for a crystalline structure to form unless there is an immense amount of nitrogen in the system [43, 52]. Another important point is that with increasing oxygen concentrations, there is a lowering of the lattice parameter caused by oxygen atoms taking the place of nitrogen in the structure [49-50]. This, in turn, causes the relaxation of internal compressive stresses and the formation of an amorphous surface [49-50].

When annealing is performed to facilitate crystallization, the analysis of the atomic concentration of nitrogen revealed oxygen’s role in stabilizing tungsten oxynitride films and coatings. With increased annealing temperatures, there was little [52] or no [49-50] loss of

nitrogen within the coatings. This indicates that oxygen does in fact help to stabilize the W-N structure at high temperatures [50, 52]. Annealing also helps bring the lattice parameter near that of bulk tungsten nitride, showing that the structure is of a W-N crystalline structure post-annealing [49].

### 1.3.3 Electro-Optical Properties

By incorporating nitrogen into  $\text{WO}_3$ , it is possible to tune the band gap and optical constants. Using UV-VIS-NIR spectroscopy analyses, researchers found that films remained at or above 80% transparent [3, 10, 43-45, 47]. However, with increased nitrogen incorporation, there is a decrease in transmittance and a redshift in absorption edge [10, 43-44, 47]. Optical constants (refractive index,  $n$  and the extinction coefficient,  $k$ ) describe the material's optical quality. Using the Swanepoel method to find  $n$  and  $k$  from the spectra transmittance data, and using ellipsometry data, authors found that both the refractive index and extinction coefficient increase with increased nitrogen incorporation or decreased with oxygen content as in Figure 1.5 [44-46]. However, the coatings were relatively thick for Swanepoel method to be effective. The increase in the refractive index is attributed to an increase in polarization due to an increase in metal-nitrogen bonds, which tend to be less polar than metal-oxygen bonds, which then leads to higher polarizability in metal nitrides [44-45]. The extinction coefficient owes its increase due to the creation of defect and absorption centers with increased nitrogen incorporation [44]. The coatings exhibit a transition from opaque to semi-transparent and finally to a transparent state with increasing oxygen flow. Within the transition zone, both the refractive index and extinction coefficient increase with increased photon energy. This is typical behavior of semi-conducting materials [46].

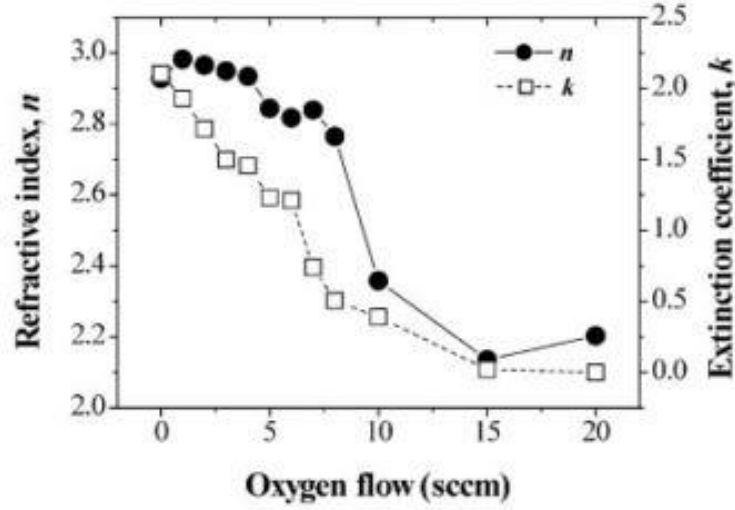


Figure 1.5: Optical constants  $n$  and  $k$  as it relates to increasing oxygen flow [46]

Of greatest importance for many authors was the analysis of UV-VIS-NIR Spectroscopy and Ellipsometry results to find the optical band gap ( $E_g$ ) as it related to the film's composition. Using either set of data by applying the Tauc-relation [10, 43, 47] or the single-oscillator model [44-45], it was observed that  $E_g$  for W-O-N thin films decreases with an increased amount of nitrogen incorporation or an increased amount of nitrogen flow during deposition as in Figure 1.6. Two explanations for this phenomenon have been presented. First Futsuhara et al. [54] suggests it's the change in ionicity due to the incorporation of nitrogen atoms. Since the electronegativity of oxygen is higher than that of nitrogen, the oxygen-metal bonds will have a higher ionicity. It can be assumed that there will be a decrease in ionicity because of the increased incorporation of nitrogen [43, 47]. The other explanation involves the formation of N 2p states above the O 2p valence state as nitrogen incorporation increases. This mixing of N 2p states and O 2p states narrows the band gap thus decreasing band gap values [43-44].

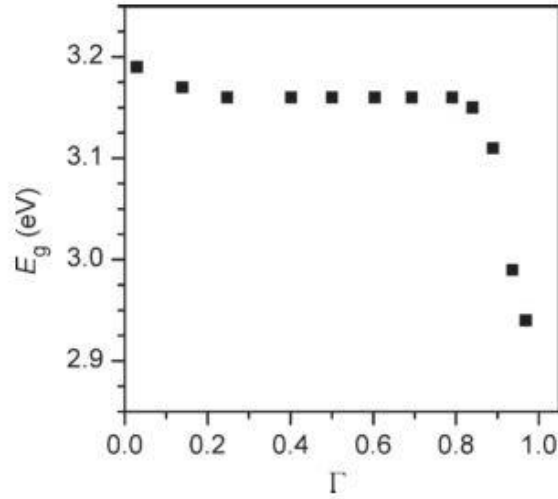


Figure 1.6: Band gap values as it relates to the normalized nitrogen partial pressure [43]

### 1.3.4 Electro-Optical Properties of Similar Metal Oxynitrides

Reviewing properties of similar metal oxynitrides will help understand the effects of annealing and a transition into a semi-absorbent condition. Much like the results for tungsten oxynitrides, but with increasing oxygen incorporation, Le Dreo et al. and Rawal et al. found tantalum and zirconium oxynitrides show that the more oxygen is incorporated into the films the greater the band gap will be [55-56]. The change in band gap describes that the reduction in grain size with increased oxygen results in higher band gap values [56]. The effect of post-annealing the films is also investigated, concluding that annealing has some effect on the optical properties of metal oxynitrides [57-58]. An interesting phenomenon in films that change from transparent (oxide like) to a semi-absorbent (nitride like) behavior, or vice versa, can be noticed from graphing  $(\alpha h\nu)^{\frac{1}{2}}$  vs.  $h\nu$ . Metal oxynitrides with this behavior exhibit two linear regions (Figure 1.7) rather than the usual single linear region [55, 58-59]. In these two examples, the material changes its optical properties, such as the band gap and insulating or semi-absorption behavior, because of a change in nitrogen or oxygen incorporation due to growth and annealing conditions.

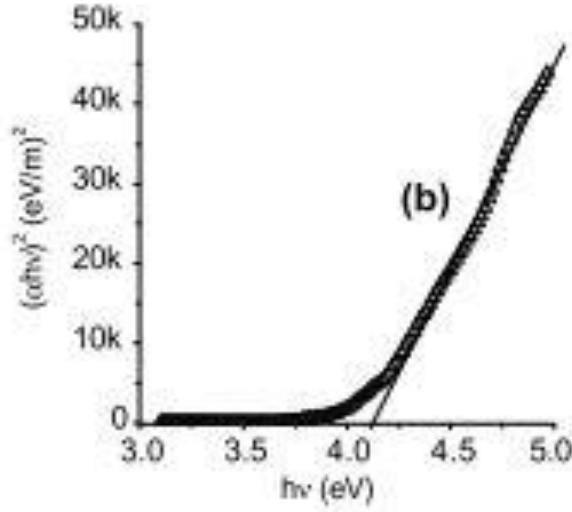


Figure 1.7:  $(\alpha h\nu)^{\frac{1}{2}}$  vs.  $h\nu$  curve of Ti-O-N exemplifying two linear regions [59]

### 1.3.5 Mechanical Properties

Shen et al. and Parreira et al. observed that with an increase of the partial pressure or flow of oxygen into the deposition chamber, the internal stresses within the coatings decreased from a compressive state [49-51]. Shen et al. also observed that before the coatings are completely free of residual stresses, the coatings are in a state of tensile stress [49-50]. The decrease in compressive stresses is explained by the replacement of nitrogen atoms by oxygen atoms, leading to lower lattice parameters, as the amount of oxygen content increases [49-50]. The coating becomes free of residual stress as the coating becomes amorphous due to a loss of intergrain coupling and increased porosity [49-51]. Along with the lower internal stresses attributed to increased amounts of oxygen, other mechanical properties are affected by the change.

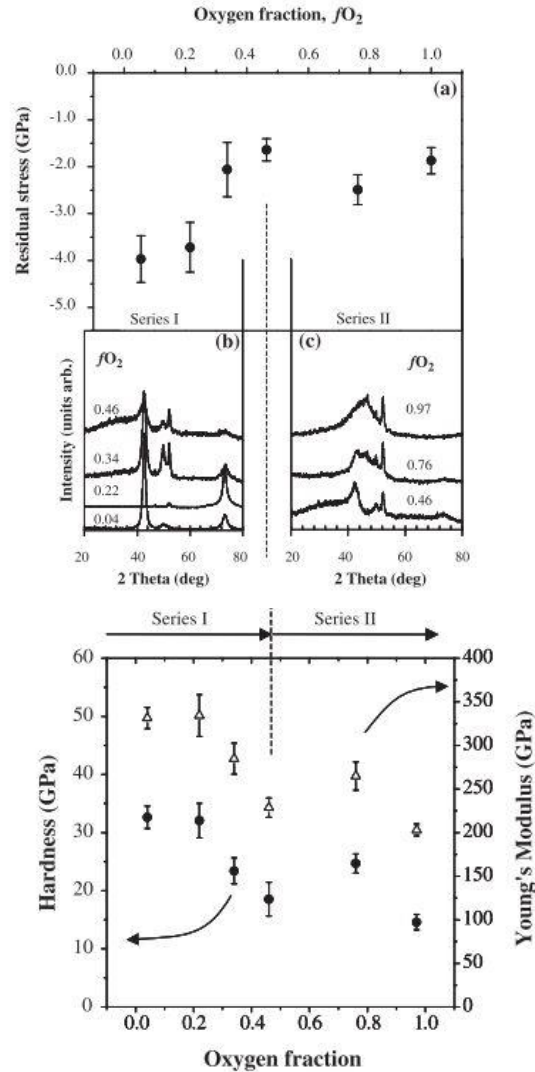


Figure 1.8: Parreira et al. show a correlation between the hardness and residual stress [51]

When compared to tungsten nitrides, tungsten oxynitrides tend to have lower hardness values. Nitrides have hardness values between 30-41 GPa and oxynitrides have values between 15-30 GPa [51-52]. This is a result of the top layer of tungsten oxide being softer than its nitride counterparts [52]. Separate studies show that tungsten oxides demonstrate even lower hardness values, only resulting in values within 7-25 GPa [14-16]. It should be noted that all of these values were gathered from samples grown on steel or alloy substrates. Within tungsten oxynitride coatings alone, the hardness of the sample seems to decrease with the amount of oxygen flowed during deposition because of the amorphous structure that is formed due to the

increased oxygen incorporation [51, 53]. But Parreira et al. show that there is a linear relationship between the hardness and residual stresses. This is exemplified when a spike in the hardness directly relates to an increase in residual stress, as can be seen in Figure 1.8 [51]. The author concludes that residual stresses within the coatings are a more dominant determinant of hardness when the coating has a crystalline structure [51].

Other mechanical attributes of tungsten oxynitrides were studied by authors to further understand the effects of oxygen incorporation and the annealing process. Shen et al. studied the density of the coatings, noticing that the density is lowered due to the amorphous nature of the coating but then annealed the sample which increased values [50]. Adhesive failure values and corrosion resistance were also analyzed and Khamseh found that tungsten oxynitrides have worse adhesion but improved corrosion resistance as compared to their tungsten nitrides counterparts [51, 53]. Also observed in studies of tungsten oxynitride coatings, was the effect that annealing conditions have on the mechanical properties of the coatings. Hardness values seem to stay consistent until the temperature reaches a certain point, then the hardness increases from 400 to 600° C (annealed for 30 minutes), then eventually drops again at the highest temperatures [52]. This eventual drop off in hardness is attributed to the outer oxide layer formed during annealing, since the hardness of oxides is low compared to the nitride phases underneath [52]. The same behavior was observed in a previous study, but instead of the correlation between hardness and annealing temperature, the study displayed a correlation between density of the coating and annealing temperature [50]. Within this study the density of the tungsten oxynitride coatings begin to increase at annealing temperatures between 400 and 700 °C, annealed for 30 minutes, then the density drops off beyond that point [50]. This is attributed to the annealing structuring the amorphous surface and leading to a less porous surface [50].

### 1.3.6 Mechanical Properties of Zirconium Tungsten Nitrides

By surveying other similar coatings we can better survey how the compositional and structural properties of coatings can affect their mechanical properties. Two separate studies by Dubey et al. show how their coatings are grown as well as the results of annealing on the mechanical properties of zirconium tungsten nitrides [60-61]. The first study, in which the effect of nitrogen flow rate during deposition is explored, it is shown that with an increasing amount of nitrogen flow, the structure of the coating changes from a single FCC phase, then an amorphous phase and lastly a dual FCC + HCP phase [60]. This clearly had an effect on the mechanical properties of the coating resulting (Figure 1.9) in the highest hardness values belonging to the coatings with a dual FCC + HCP structure, followed by the coatings with the FCC phase structure then the amorphous coatings [60].

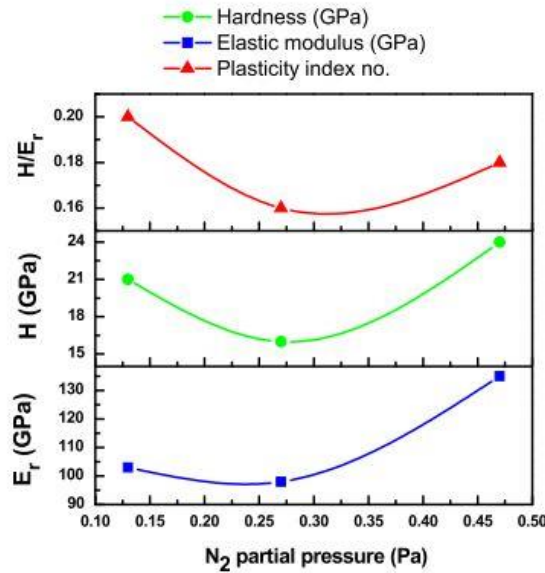


Figure 1.9: Mechanical properties of Zr-W-N at FCC, amorphous then FCC + HCP structures [60]

The other study by the same group explored the effect that post-deposition annealing on the mechanical properties of amorphous coatings. Amorphous coatings were annealed from 100 to 600° C and resulted in coatings that remained amorphous in structure evident through

broadening of weak peaks in the XRD patterns, likely due to oxygen atoms involved in atomic diffusion, structure conversion and inducing stresses in the coatings [61]. Since the coatings were annealed in the presence of air, oxygen began to become incorporated into the coatings at an annealing temperature of 300° C [61]. As the annealing temperature raised so did the amount of oxygen incorporation, causing a decrease in hardness values as oxygen incorporation increased [61].

## **Chapter 2: Literature Review**

### **2.1 WORKS PUBLISHED ON TUNGSTEN OXYNITRIDES**

Most works published on the subject of tungsten oxynitrides thin films and coatings are aimed at gathering results on the structure and optical properties of W-O-N coatings. Furthermore, the results available literature deals mostly with the relatively thicker coatings but relation to the reduced dimensionality (such as nano/micro scale) is missing. In fact, majority of the previous attempts were aimed at forming a relation between structural and compositional properties. Only a few selected publications on W-O-N coatings discusses mechanical properties and none discuss any relation between optical data and trends seen in the outcome mechanical testing. In either case, the formation of W-O-N promises to enhance tunability and improve the functionality of the application envisioned for the film or coating. While most of the results available in the literature are already discussed in the previous chapter, the following sections summarize information specifically those on the tungsten oxynitride coatings.

#### **2.1.1 Electro-Optical Properties**

The first of many significant works on tungsten oxynitride thin films authored by Mohamed et al. centers around W-O-N thin films with a low concentration of nitrogen incorporation for the purpose of tuning structural, optical and electrical properties for temperature dependent resistors, diffusion barriers and gate material [43]. The study resulted in decreased band gap and resistivity as the partial pressure ratio of nitrogen increased [43]. Later studies, by Mohamed et al. and Parreira et al., expanded the composition of tungsten oxynitrides to include higher concentrations of nitrogen [44, 46]. The study published by Mohamed et al. was to find the composition, structural and optical properties to enhance the films for use in heterogeneous catalysis for hydrogen transfer reactions and for capacitor barrier layer in memory cells and their apparatus resulting in a higher index of refraction in nitrogen doped tungsten oxide films [44]. Expanding on their own results, Mohamed et al demonstrated the effect of composition on amorphous tungsten oxynitride films, resulting in decreasing optical band gap

and increasing index of refraction with nitrogen incorporation [44-45]. The works by Mohamed et al. are also of significance for their use of the Wemple and DiDomenico (WDD) dispersion relationship model to find the energy dependence of the index of refraction to describe the optical band gap and chemical bonding within the film [44-45].

Subsequent publications have attempted to fine tune optical properties by either changing the deposition parameters or the structure of the films. Chawla et al. conducted a study with the goal of extending “light harvesting capability to a wider portion of the solar spectrum” and found that nitrogen doping of tungsten oxide does, in fact, lower the band gap [10]. The study demonstrated that deposition in a helium atmosphere, compared to an argon atmosphere, results in ever lower band gap values [10]. Other properties, important for different electro-optical applications, including electrochromic properties and film resistivity were also explored. Nakagawa et al. went on to explore electrochromic properties of nitrogen doped tungsten oxide films for use in “smart window” technology, variable reflectance mirrors and display devices; they concluded that the addition of nitrogen changed electrochromic coloration from blue to black [3]. Expanding on this work, Sun et al. published a work showing the structural, morphological, electrochromic and lithium insertion properties of nitrogen doped tungsten oxides [47]. Finally, Vemuri et al. attempted to manufacture rf-sputtered low resistive nitrogen doped tungsten oxide films, “with fundamental absorption shifted to longer wavelengths”, and concluded that the conductivity of said films is lowered with increased nitrogen content [48].

### **2.1.2 Mechanical Properties**

Most of the available data in the literature is pertinent to tungsten nitrides only. Shen et al., concentrated on the effects of oxygen incorporation on tungsten nitride coatings to improve the thermal stability for high temperature diffusion barriers [49-50]. The authors believe that oxygen atoms would be incorporated into grain boundaries of the tungsten nitride coating and help block diffusion paths; results showed that tungsten oxide over-layers did improve thermal stabilization of the tungsten nitride phases ( $W_2N$ ) [49-50]. Later publications focused on

properties of tungsten oxynitrides that would improve mechanical properties for hard coatings over those of tungsten nitrides by improving thermal stabilization. Parreira et al. conducted a study, where hardness of tungsten oxynitride coatings decreased with the increase of oxygen incorporation into the system [51]. Louro et al. conducted a study with a similar goal of improving wear resistant hard coatings, but with added durability at elevated temperatures [52]. This study also attempted to form a tungsten oxide top layer, or over-layer; instead of blocking diffusion pathways the goal was to delay the oxidation process since tungsten nitrides alone have a low oxidation threshold temperature [52]. The study showed that the  $W_2N$  phase remained stable at 800 °C in oxynitride coatings, whereas the  $W_2N$  phase deteriorated in the un-doped tungsten nitride coating at the same temperature and the overall hardness improved post-annealing up to annealing temperatures of 600 °C [52]. Most recently, Khamseh conducted a study on the corrosion resistance of tungsten oxynitride, combining the corrosion resistance of tungsten oxide with the mechanical properties of tungsten nitrides [53].

## **2.2 GOALS AND OBJECTIVES OF PRESENT WORK**

It is now clear from the discussion presented in Chapters 1 and 2 that  $WO_3$  is a widely studied “chromogenic” material with interesting structural, electronic, and optical properties for utilization in many scientific and technological applications. Coupled with good electronic transport properties, photosensitivity, and chemical integrity,  $WO_3$ -based materials are attractive for applications related to sustainable energy production including energy efficient windows and architecture, photoelectrochemical water-splitting, photocatalysis, and solar cells. On other hand,  $WO_3$  is a complex material, with respect to crystal structure and thermal stability, as a result of the high degree of polymorphism exhibited by both stoichiometric and non-stoichiometric W oxides. Both stoichiometric and non-stoichiometric W-oxide based materials are, therefore,

quite important and offer a platform to further investigate the fundamental structure-property relationships for utilization in optical and electronic device applications.

The goal of the present work is to derive a fundamental knowledge in terms of the comprehensive understanding of the structure, physical, chemical, optical and mechanical properties of W-O-N nano-coatings and establishing a structure-property relationship. The W-O-N, the focus of the present work, belongs to a family of materials, which can be represented chemically by  $\text{MO}_x\text{N}_y$ , or M-O-N, which in turn can offer advantages over the nitride-oxide end members, providing the ability to tune the desired properties based on the chemical composition. Oxynitrides can also combine the traditional advantages of nitrides, such as oxidation resistance and structural stability at elevated temperatures. Keeping these points in mind, this thesis work has been directed to the fabrication and property evaluation of tungsten oxynitride nano-coatings. The benefits of the present work many fold. For instance, compared to work reported on Ti-based oxynitrides, studies focused on W-oxynitrides are meager. Therefore, the present work fills a fundamental knowledge gap in terms of establishing a comprehensive understanding of the structure, physical, chemical, optical and mechanical properties of W-O-N nano-coatings and establishing a structure-property relationship. The other point of significance is as follows. While earlier efforts were focused on either thicker coatings (several microns) or a specific phase, where complications arise when nitrogen induced amorphization leads to reduced thickness or structural effects, the present work is focused towards understanding the effect of nitrogen content in reactive sputter-deposition of amorphous W-O-N films for a set of samples with controlled film thickness of 100 nm.

This study also aims to expand the base of knowledge for the mechanical properties of tungsten oxynitrides, since there are a limited number of similar studies; especially of samples

with a high oxygen fraction as stated by Parreira et al. [51]. Only three of the reviewed articles, authored by Louro et al., Parreira et al. and Khamseh, have dealt directly with obtaining hardness and Young's modulus values for tungsten oxynitrides [51-53]. The combination of mechanical properties and electro-optical properties within the same study is not seen within the literature, especially for amorphous films and coatings, and will give insight into how to best optimize tungsten oxynitrides for real practical or industrial device applications. The specific objectives of this present study are outlined below, but are focused at the characterization and analysis of optical and mechanical properties of tungsten oxynitride thin nano-coatings with a range of compositions, accomplished by varying the ratio of nitrogen and oxygen introduced into the vacuum chamber during deposition.

1. Fabricate amorphous tungsten oxynitride ( $\text{WO}_x\text{N}_y$ ) nano-coatings with  $\sim 100$  nm thickness with a range of elemental compositions onto silicon and quartz substrates.
2. Characterize the structure and surface morphology of the coatings before and after post-annealing treatment to understand the role that these characteristics have in affecting optical and mechanical properties.
3. Determine the elemental compositions of the coatings before and after post-annealing treatment to enable the formation of any relation between the coating's composition and the trends seen in the optical and mechanical properties.
4. Analyze optical characterization to determine the band gap and other properties to ensure the formation of high quality coatings that are easily tunable and reproducible.
5. Propose an electronic structure model that accounts for all changes in composite-like semiconducting optical behavior as it relates to the composition of the coatings.
6. Determine the hardness and Young's modulus of the coatings using a non-destructive method of testing that ensures the measurement of only the coating without influence of the substrate.

## **Chapter 3: Methodology**

### **3.1 DC SPUTTERING DEPOSITION**

Tungsten oxynitride coatings were fabricated by sputter-deposition, which is a physical vapor deposition method widely utilized in the manufacturing of microelectronic components. Coatings in this work were made by direct current (DC) sputtering because it allows control to the user, enabling him or her to specify the structure, composition, and thickness of the coating. To perform sputtering deposition, surface atoms are ejected, from the target and onto the substrate, by momentum transfer by other atomic sized, energetic, particles. Normally ‘sputtering’ is a non-thermal vaporization process without any chemical reactions. Sputtering Decomposition itself has many different methods and can either be plasma based ( $10^{-1}$  to 10 Pa) or ion based ( $10^{-5}$  to  $10^{-2}$  Pa) [62].

When using DC sputtering deposition the target and substrate are placed onto a diode or two parallel electrodes attached to the power supply. The target and substrate are both placed within a vacuum chamber which is then filled with an inert gas, usually argon and or nitrogen. When the DC voltage is applied to the diode, the target being the cathode and the substrate as the anode, free electrons accelerate and collide with the inert gas. This will cause a plasma discharge and a “dark space” near the target [63]. Ions entering the dark space bombard, or sputter, the target and atoms locked out from the target transport towards the substrate. This final step, the transportation of atoms to the substrate, consists of those atoms that are to coat the substrate and become the coating layer. Compounds can be formed by the process of reactive sputtering by sputtering targets in an atmosphere that includes reactive gasses such nitrogen and oxygen that will be deposited along with the target material.

### **3.2 CHARACTERIZATION METHODS**

#### **3.2.1 X-Ray Diffraction**

X-ray diffraction analysis (XRD) and scanning electron microscopy (SEM) were used to analyze the structure and surface morphology, respectively. XRD is an extremely valuable tool

that describes the material's crystal structure as well as mechanical properties such as the internal stresses within the coating itself. The basis of XRD analysis begins with the principle of constructive interference that is to say when X-rays are deflected, off of a sample, at equal angles and satisfying the necessary conditions. The conditions were described according to Bragg's law, which is:

$$n\lambda = 2d\sin\theta \quad (1)$$

where  $n$  is an integer describing the number of wavelengths,  $\lambda$  is the wavelength of the incident radiation,  $d$  is the inter-planar spacing between periodic planes of atoms and  $\theta$  is the angle of diffraction. When the conditions are satisfied the X-rays that are scattered from the sample will interfere constructively and become a diffracted beam. If more X-rays are deflected by atoms that are in the same plane, the intensity of the diffracted beam will increase. This results in a diffraction pattern, or diffractogram, where peaks in the pattern describe the structure of the coating and what elements exist. However XRD is limited by the angle at which it sends X-rays to the surface of the sample making it sometimes difficult to detect coatings on a relatively much thicker substrate. To determine the structure of the coating and to obtain reliable information, grazing incidence x-ray diffraction (GIXRD) is employed to characterize W-O-N nano-coatings in this work. GIXRD uses X-rays at much smaller entrance angles that result in longer pathways for the diffracted beams to travel, thus resulting in better resolution for nano-coatings.

### 3.2.2 X-Ray Photoelectron Spectroscopy

For analysis of the elemental composition of the coatings, X-ray photoelectron spectroscopy (XPS) can be used as a quantitative spectroscopic technique to measure the composition and empirical formula, as well as the chemical and electron states. XPS spectra are obtained by irradiating the sample with an Al or Mg X-ray and synchrotron source and measuring the kinetic energy and number of electrons that escape from the top 1 to 10 nm of the sample [64]. Required for making such measurements is a fixed energy X-ray, electron energy analyzer capable of measuring the flux of electrons according to their particular energy and a

vacuum environment in order to avoid any unwanted particle collisions. Using this method the binding energy ( $E_{binding}$ ) of the emitted electrons can be determined using the equation below, first developed by Ernest Rutherford [64].

$$E_{binding} = E_{photon} - E_{kinetic} - \Phi \quad (2)$$

In equation 2;  $E_{photon}$  is the energy of the X-ray source photons,  $E_{kinetic}$  is the energy of the emitted electrons and  $\Phi$  is the work function of the spectrometer. Each element has its own characteristic peaks at specific binding energies, indicating the existence of said element within the coating, if present. These peaks correspond to the electron configuration, with the atoms and the intensity of the peaks indicating the concentration of the element within the coating.

### 3.2.3 Rutherford Backscattering Spectrometry

Rutherford backscattering spectrometry (RBS) was also used to determine the elemental composition of the samples to further understand the effects of nitrogen content on the properties of tungsten oxynitrides. RBS uses a detector to measure the number and energy of ions that are backscattered after colliding with the atoms on the near-surface of a sample [64]. To obtain the composition of a thin film or nano-coating it is usually required to have ion source or proton source, generated by a particle accelerator. It is then important to rotate the sample, using a goniometer, so that the compositional depth profile can be obtained. Lastly, a detector is used to measure the energy of the ions backscattered across the range of angles. This analysis results in an energy spectrum which is analyzed for composition using a program such as SIMRA to compare computer simulations of the spectra to the experimental data gathered [65-66]. Below in Figure 3.1, is a schematic of the experimental setup used commonly to conduct RBS analysis.

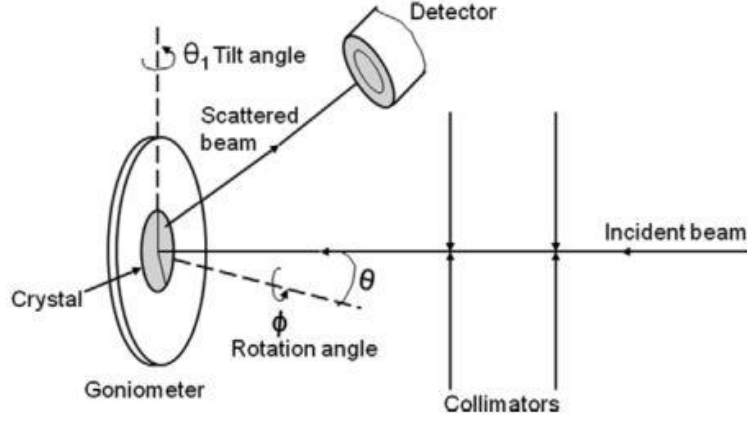


Figure 3.1: Schematic of RBS experimental setup [64]

### 3.2.4 UV-VIS-NIR Spectroscopy

Spectral characteristics of tungsten oxynitride nano-coatings were examined by the ultraviolet–visible–near infrared spectroscopy (UV-VIS-NIR Spectroscopy). In order to perform UV-VIS-NIR spectroscopy, a source of light with a range between the ultraviolet and near-infrared portion of the spectrum, is separated into individual wavelengths of light. This light is then separated into two separate beams, which are separately targeted at a reference sample, usually made of the substrate material, and at the sample itself. After passing through the sample, the remaining light is measured for light intensity by separate detectors. The ratio of the light intensity passing through the sample to the intensity of light through the reference substrate, which should be near full intensity, is the measurement of transmittance for the sample being analyzed. This set of data can then be used to find the band gap, which is the energy needed to excite an electron into a state in which it can participate in conduction, or the difference in energy between the conduction and valence band in a semiconducting or insulating material. By using “Tauc’s Relation”, as seen in Equation 3,

$$(\alpha h\nu) = B(h\nu - E_g)^2 \quad (3)$$

where  $\alpha$  is the absorption coefficient,  $h\nu$  is the energy of the incident photon,  $B$  is the absorption edge width parameter and  $E_g$  is the band gap; we can find the value of the band gap for each

sample tested [43-45, 56-58, 67]. The “Lambert-Beer Law” (Equation 4) can then be used to find the value of the absorption coefficient using the data from UV-VIS-NIR Spectroscopy,

$$\alpha = -\frac{\ln(T)}{t} \quad (4)$$

in which  $T$  is the measured transmittance and  $t$  is the thickness of the sample being analyzed [43, 45, 57, 67]. The final step to find the band gap is to plot  $(\alpha h\nu)^{\frac{1}{2}}$  vs.  $h\nu$  and the linear region of the plot is then extrapolated to  $h\nu = 0$  resulting in the value of the samples optical band gap [43, 45, 56-58, 67].

### 3.2.5 Ellipsometry

Ellipsometry is used to explore the optical properties of coatings. By measuring the change in polarization, in terms of amplitude ratio ( $\psi$ ) and phase difference ( $\Delta$ ), between a light source of known polarization and that of the light reflecting off of the sample, the thickness and optical constants, at different wavelengths of light, can be found along with band gap values. The optical constants are as follows: the refractive index ( $n$ ) describes the speed at which light propagates through a sample compared to the speed of light through a vacuum, and the extinction coefficient ( $k$ ) helps to describe how light is absorbed in the sample. To find the optical constants and other optical data such as the band gap ( $E_g$ ) from the given data, a model analysis has to be performed to fit calculated values of  $\psi$  and  $\Delta$  with the experimental data to find the thickness and optical properties of the coatings. The models used in the current study are described in the Results section.

### 3.2.6 Nano-Indentation

Nano-indentation tests are performed to find the hardness and Young’s modulus of each sample. This analysis allows us to determine the mechanical behavior of tungsten oxynitride nano-coatings. In a method described by Oliver and Pharr [68], the elastic modulus (Young’s modulus) and hardness of a coating can be ascertained from the relation between the load and

displacement of an indenter during continuous loading and unloading, as can be seen in Figure 3.2.

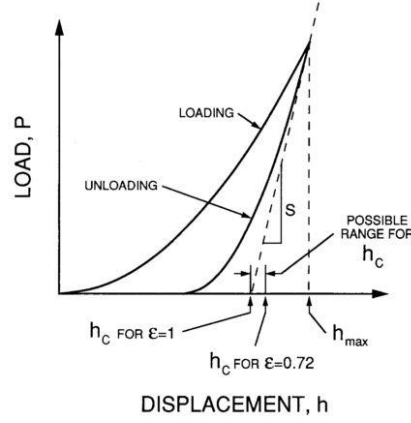


Figure 3.2: Typical Load vs. Displacement graph [68]

The first step is to account for the non-rigidity of indenters. This is done by forming Equation 5, and solving for the term  $E_r$  or reduced modulus.

$$\frac{1}{E_r} = \frac{1 - \nu^2}{E} + \frac{1 - \nu_i^2}{E_i} \quad (5)$$

In Equation 5,  $E$  and  $\nu$  describe the Young's modulus and Poisson's Ratio for the sample while  $E_i$  and  $\nu_i$  represent the same parameters but for the indenter. The next step is to define the expression for  $E_r$  as it would relate to the stiffness ( $S$ ) of the sample during unloading, as shown in Equation 6.

$$E_r = \frac{\sqrt{\pi}}{2} \frac{S}{\sqrt{A}} \quad (6)$$

The next step is to define  $A$ , the area of contact at peak load. If an area function is defined experimentally with respect to the contact depth ( $h_c$ ), then solve for the term  $h_c$ .

$$A = F(h_c) \quad (7)$$

The contact depth is defined by Equation 8, and since  $h_{max}$  is known experimentally, the contact perimeter,  $h_s$ , is then left to be defined.

$$h_c = h_{max} - h_s \quad (8)$$

The contact perimeter is then defined with a geometric constant,  $\varepsilon$ , to take into account the shape of the indenter.

$$h_s = \varepsilon \frac{P_{max}}{S} \quad (9)$$

Oliver and Pharr took into account the fact that the unloading data isn't a linear relation, and the data was fit by a simple power law relation, as can be seen by Equation 10.

$$P = A(h - h_f)^m \quad (10)$$

When the curve is fit using the least squares fitting method, the constants  $A$ ,  $m$  and  $h_f$  are all determined. The equation is then derived at the maximum load and displacement, to solve for the slope of the unloading curve giving us the stiffness,  $S$ . From this point, all of the necessary unknowns are accounted for and the final Young's modulus for the sample is known from the data. To find the hardness values, the same value for area of contact is used along with the maximum load, as shown by Equation 11.

$$H = \frac{P_{max}}{A} \quad (11)$$

### 3.3 DEPOSITION

To best understand how structure, composition and post-annealing all affect the electro-optical and mechanical behavior of tungsten oxynitrides, several samples were grown to optimize these properties. The samples were fabricated using physical vapor deposition, specifically direct current (DC) sputtering with a 2" diameter W-target of 99.94% purity, onto silicon (Si) (100) and optical grade quartz substrates. An Advanced Energy MDX 500 DC power supply provided power to the sputtering gun which was placed at a distance of 80 mm from the substrates. Before deposition, RCA (Radio Corporation of America) cleaning was employed for the silicon substrates. Quartz substrates were cleaned with isopropanol and all substrates were dried before introduction into the vacuum chamber. The deposition chamber was evacuated to a base pressure of  $\sim 3.0 \times 10^{-7}$  Torr before deposition took place, and 20 sccm of argon was flowed into the chamber once adequate base pressure was reached then, 100 Watts of power was supplied to ignite the plasma. For reactive deposition of W-O-N nano-coatings,

oxygen and nitrogen were employed along with Argon. Total gas flow was kept at a constant 40 sccm, resulting in a working pressure of 10 mTorr at a pumping speed of 50 L/s. The ratio of argon to reactive gases was kept equal with a total flow of 40 sccm. The reactive gases, oxygen and nitrogen, were kept at a combined 20 sccm and the ratio of oxygen to nitrogen was varied in order to understand the effects of nitrogen content on the physical, mechanical and optical properties of W-O-N coatings. The conditions used for deposition are summarized in Table 3.1. Pre-sputtering was performed using Ar, with the gun shutter closed, for 10 minutes before the substrate was exposed for deposition. All depositions were carried out at room temperature (25 °C). Deposition took place for the length of time required to reach a thickness of  $\approx 100$  nm, as measured by in situ ellipsometry.

Table 3.1. Sputtering conditions employed for the deposition of W-O-N nano-coatings.

<b>Physical Parameter</b>	<b>Set Value</b>
Base pressure	$3 \times 10^{-7}$ Torr
Sputtering power	100 W
Processing gases	Ar, N <sub>2</sub> , O <sub>2</sub>
Substrates	Silicon and quartz
Deposition temperature	Room temperature (25 °C)
Target-to-substrate distance	8 cm
Total gas flow	40 sccm (constant)
Ar gas flow	20 sccm (constant)
N <sub>2</sub> gas flow	0-20 sccm (variable)
O <sub>2</sub> gas flow	0-20 sccm (balanced)
Working pressure	10 mTorr
Pumping speed	50 L/s
Deposition rate	20 nm/min
Coating thickness	100 nm

## Chapter 4: Results and Discussion

### 4.1 STRUCTURAL PROPERTIES

Grazing incidence x-ray diffraction (GIXRD) was used to minimize any interference from the substrate and to obtain structural information about the coatings alone. The GIXRD patterns of W-O-N nano-coatings are shown in Figure 4.1. From the GIXRD patterns in Figure 4.1 of the W-O-N coatings, it can be seen that all of the samples are amorphous in the entire range of nitrogen gas flow rates used for fabrication. Absence of peaks in the patterns is a clear indication of amorphous nature of the samples. Because of the absence of any additional energy during deposition, no discernable peaks are observed, indicating that no crystalline structures exist to create constructive interference in the GIXRD patterns. Normally, additional substrate heating or substrate bias voltage is employed to supply energy during deposition. Since neither of these methods was employed, the period of the atomic jump process of adatoms is very large and condensed species may stay stuck to the substrate surface region where they land leading to an amorphous coating. Insufficient thermal or electrical energy thus would not provide enough energy to promote any structuring, or “phase ordering”, of oxide or nitride phases within the coatings [49]. Shen et al. have reported that tungsten oxynitride amorphous films, which are obtained by using a different set of processing parameters, will remain unstructured even after post thermal treatment of insufficient temperature [49].

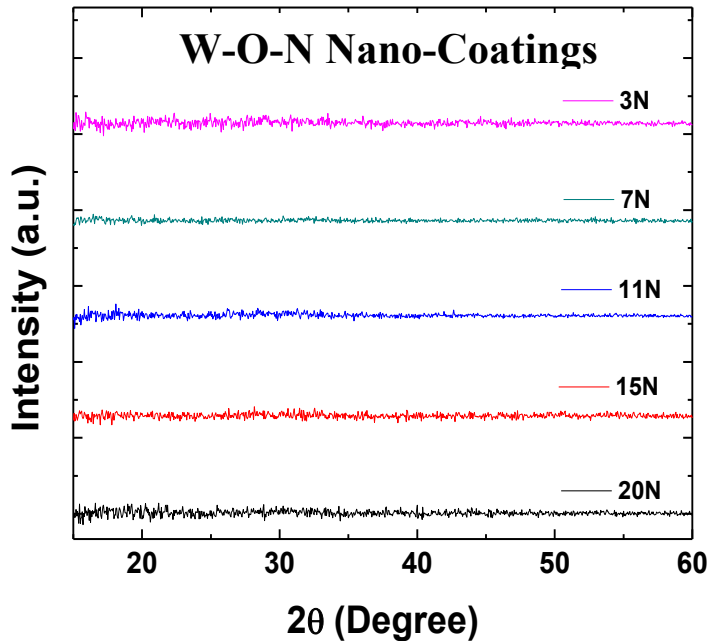


Figure 4.1: GIXRD patterns of W-O-N nano-coatings deposited at various nitrogen gas flow rates. The amorphous nature of the W-O-N coatings is evident from the patterns.

## 4.2 CHEMICAL COMPOSITION

In order to describe any optical or mechanical behavior that may be observed, it is fundamentally necessary to obtain a chemical information of the W-O-N coatings. XPS and RBS measurements were made on the W-O-N coatings as a function of nitrogen content. The XPS survey spectra of W-O-N coatings are shown in Figure 4.2. The XPS survey spectra displays the elements present in the W-O-N coatings deposited as a function of nitrogen flow rate. The elements present in the coating grown with 9 sccm of nitrogen flow in the binding energy (BE) range of 0-600 eV are seen in Figure 4.2. Present in the sample are the elements W, O and N that are attributed to the constituent elements present in the samples and represented by the W 4f, O1s and N1s peaks in their respective BE positions indicated in Figure 4.2. Carbon is present on the surface of the coating due to the absorption of hydrocarbons to the coating's surface during transfer from the growth chamber to the XPS instrumentation. The W-O-N coating had

sufficient thickness and sufficient coverage of the entire substrate surface to prevent detection of the photoelectrons from the substrate.

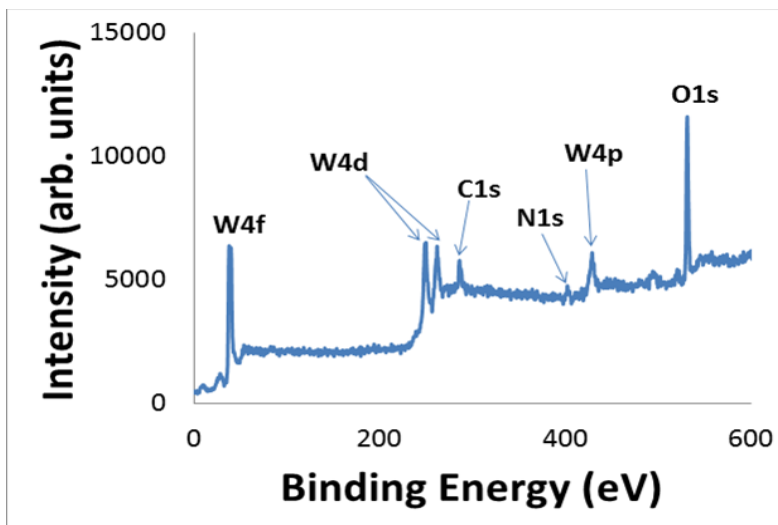


Figure 4.2: XPS survey spectrum of W-O-N nano-coatings deposited with 9 sccm of nitrogen flow

To gain an insight of how the flow of nitrogen flow affected the nitrogen uptake during deposition, the N 1s core level peak was recorded and analyzed further. The N 1s peak stack plot is displayed as a function of nitrogen flow rate in Figure 4.3. The N 1s peak intensifies (Figure 4.3a), indicating a steady increase in nitrogen content as the flow of nitrogen gas is increased. The peak area for the N 1s peak, as determined by the peak fitting procedure described earlier, is displayed in Figure 4.3b. It can be seen from this analysis that the peak area for nitrogen increases dramatically for nitrogen flow rates of 9 sccm and greater indicating a shift in composition, likely a shift in the coating's optical and mechanical properties.

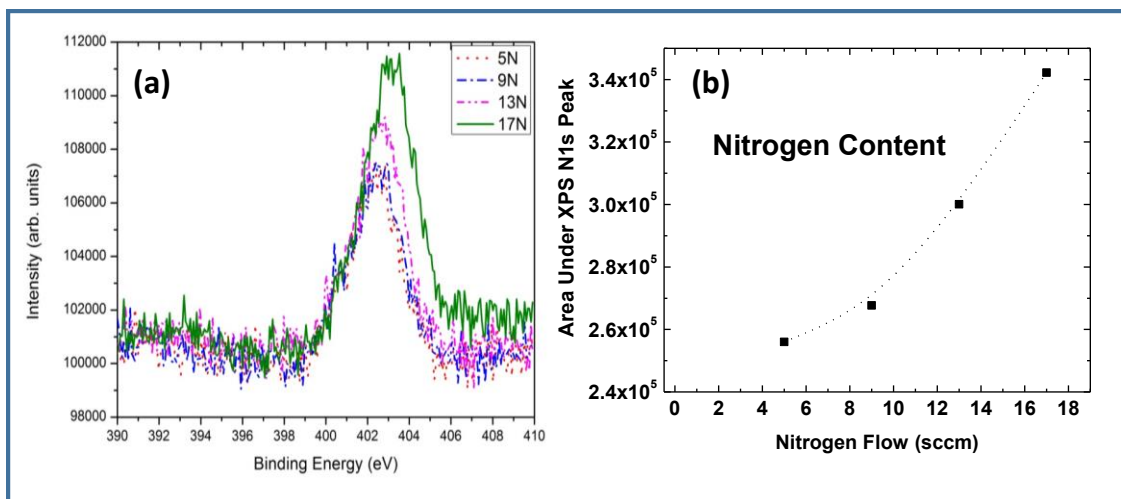


Figure 4.3: N 1s peak evolution as a function of nitrogen gas flow rate (a) and the area of the N 1s peak obtained via peak fitting of the high resolution XPS spectra (b)

RBS measurements were gathered to quantify the elemental composition of the W-O-N nano-coatings. Both the experimental curve (circles) and simulated curve (lines) are present in the RBS spectra for two compositions of W-O-N coatings displayed in Figure 4.4.

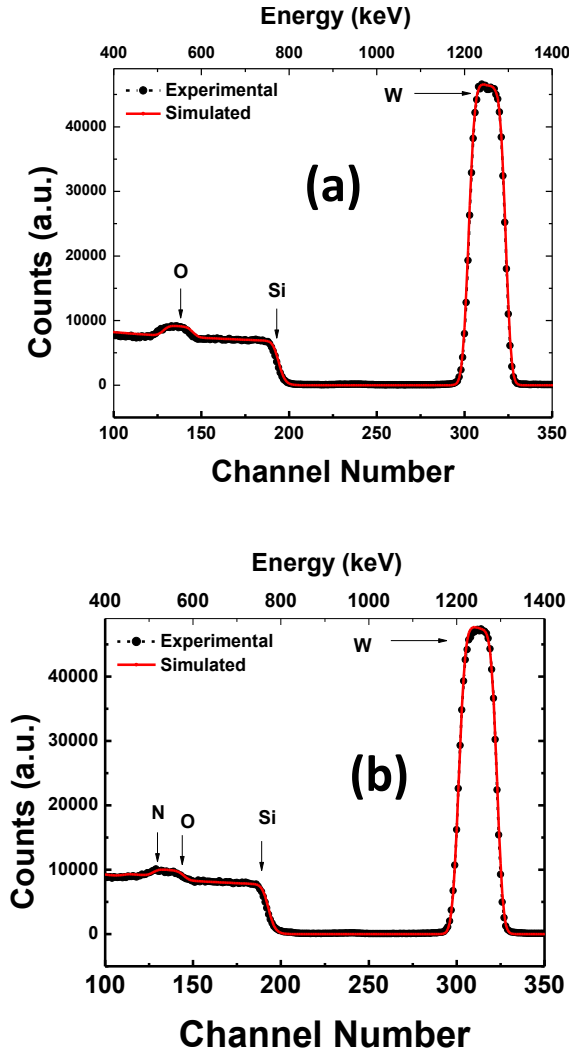


Figure 4.4: RBS spectra of W-O-N nano-coatings with both experimental and simulated (SIMNRA) data shown for the samples of pure  $\text{WO}_3$  deposited with no nitrogen (a) and W-O-N deposited with 9 sccm of nitrogen flow (b)

The various elements present, and their respective energy position, are indicated in the spectra by arrows. The heaviest of the elements, W, occurs at higher backscattered energy and the other elements present (Si, O, and N) are shown in the RBS spectra as well. Using SIMNRA code [65], it was possible to calculate the simulated curve of the RBS spectra for the fixed set of experimental parameters: (1) incident  $\text{He}^+$  ion energy, (2) integrated charge, (3) energy resolution of the detector, and (4) scattering geometry. The outcome of the calculations, seen in Figure 4.4, agree with the experimental RBS spectra and indicate that the simulation is fit to

estimate the coating composition. Figure 4.4a indicates that the coatings grown without nitrogen correspond to stoichiometric  $\text{WO}_3$  (W:25% and O:75%), as can be seen by the lack of any nitrogen in the RBS spectra. Most significantly, however; RBS measurements indicate that no significant nitrogen incorporation takes place in samples deposited with nitrogen flow rates  $\leq 9$  sccm, as also specified by XPS analysis. Figure 4.4b shows the RBS spectra for the W-O-N nano-coatings with 9 sccm of nitrogen flow, and it can be gathered that nitrogen begins incorporation from this point and RBS data estimates composition to be  $\text{WO}_{2.60}\text{N}_{0.40}$ . From this point, RBS data confirms the steady increase in nitrogen content, with corresponding oxygen content being decreased as a result. The final compositions, also indicated in Table 4.1, for the W-O-N nano-coatings are sequenced as follow:  $\text{WO}_3 \rightarrow \text{WO}_{2.60}\text{N}_{0.40} \rightarrow \text{WO}_{2.48}\text{N}_{0.52} \rightarrow \text{WO}_{2.20}\text{N}_{0.8}$ .

Table 4.1: Chemical composition of W-O-N nano-coatings as calculated by SIMNRA from the RBS spectra as a function of nitrogen flow

$\text{N}_2$ flow rate (sccm)	Composition
5	$\text{WO}_3$
9	$\text{WO}_{2.60}\text{N}_{0.40}$
13	$\text{WO}_{2.48}\text{N}_{0.52}$
17	$\text{WO}_{2.20}\text{N}_{0.80}$

### 4.3 OPTICAL PROPERTIES

The spectral transmission characteristics of W-O-N nano-coatings are shown in Figure 4.5. As gathered by UV-VIS-NIR Spectroscopy, the optical transmittance spectra for the W-O-N coatings, as seen in Figure 4.5, show a gradual change in the spectral transmission curves as the nitrogen flow of the coatings is increased. The coatings show a region of high transparency across the spectral region between 250 and 800 nm before being affected by absorption across the band gap ( $E_g$ ) in lower wavelengths. Other observations from the optical transmittance spectra are a red-shift in spectral absorption, as illustrated by the arrow in Figure 4.5, and an

overall decrease in spectral transmittance. Both observations can be seen to be a function of nitrogen content, indicating an incremental change in the coating's electronic structure as nitrogen content is increased; especially after the significant incorporation at 9 sccm of nitrogen flow rate seen in the compositional analysis. As a result of these observations, further investigation into the electronic structure, as it relates to the band gap and the optical properties of the W-O-N coatings, are to be performed by using ellipsometry functions and Tauc-Lorentz (TL) modeling.

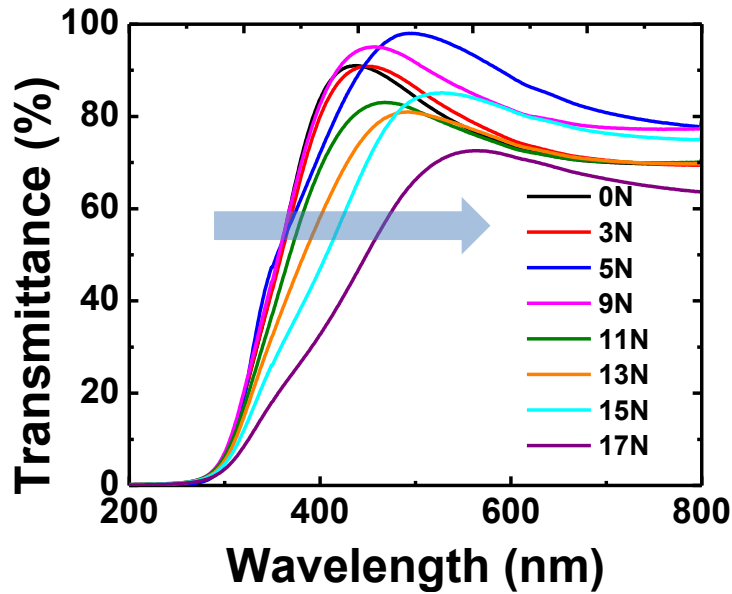


Figure 4.5: Optical spectral transmittance curves at various nitrogen flow rates. A shift in absorption can be seen with increasing nitrogen flow rate and is indicated by the arrow.

The optical constants of W-O-N coatings were determined from spectroscopic ellipsometry (SE), which measures the relative changes in the amplitude and phase of the linearly polarized monochromatic incident light upon oblique reflection from the sample surface. The experimental parameters obtained by SE are the angles  $\Psi$  (azimuth) and  $\Delta$  (phase change), which are related to the microstructure and optical properties, by:  $\rho = R_p/R_s = \tan\Psi \exp(i\Delta)$ , where

$R_p$  and  $R_s$  are the complex reflection coefficients of the light polarized parallel and perpendicular to the plane of incidence, respectively.

The primary step in SE data analysis and derivation of optical constants is constructing the optical stack model of the sample. In Figure 4.6, a schematic of the optical stack model representing the W-O-N nano-coatings constructed in order to simulate the spectra for determining the optical constants is represented. From top to bottom, the model contains the W-O-N coating, followed by a  $\text{SiO}_2$  interface and finally the Si substrate. Also included in the model is interfacial and surface roughness in order to increase the accuracy of the results obtained by the analysis.

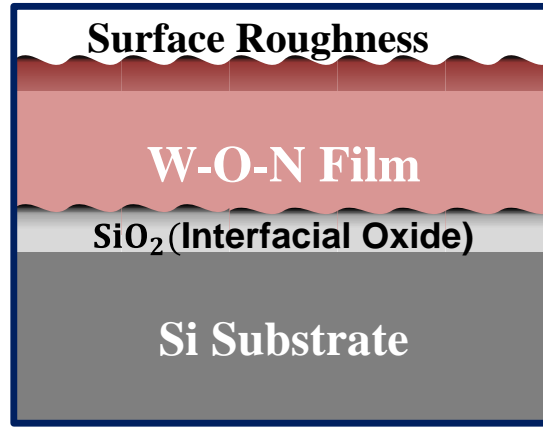


Figure 4.6: Optical stack model of W-O-N nano-coatings used for ellipsometry data analysis

After constructing the optical stack model, the Tauc-Lorentz (TL) oscillator was used to determine the values for the band gap as well as  $n$  and  $k$ . The empirical parameterization is based on the Tauc expression for the imaginary part ( $\epsilon_2$ ) of the dielectric function [69, 71-73]. The complex dielectric function  $\epsilon_2$ , for a single transition, is represented in Equation 12 [71-73]:

$$\epsilon_2(E) = \left[ \frac{AE_0 C (E - E_g)^2}{(E^2 - E_0^2)^2 + C^2 E^2} * \frac{1}{E} \right] \quad (12)$$

where  $E_0$  is the resonance energy,  $E_g$  represents the band gap energy,  $E$  is the photon energy and  $A$ ,  $C$  are the amplitude coefficient and broadening coefficient of the  $\varepsilon_2$  peak. It should be noted that both the real and imaginary parts of the dielectric functions can be related to  $n$  and  $k$  by setting  $\varepsilon_1 = n^2 - k^2$  and  $\varepsilon_2 = 2nk$ . It has been shown that the TL model is effective at modeling the optical properties of transparent oxides [6, 69-70, 74-75]. Seen in Figure 4.7 the spectral dependencies of the ellipsometric parameters ( $\psi$  and  $\Delta$ ), as determined for the W-O-N coatings with increasing nitrogen flow, fit well with the simulated data as determined by the TL model and minimized by the Levenberg-Marquardt algorithm described below in Equation 13,

$$MSE = \frac{1}{2N - M} \sum_{i=1}^n \left[ \left\{ \frac{\psi_{exp.} - \psi_{calc.}}{\sigma_{\psi_i}^{exp}} \right\}^2 + \left\{ \frac{\Delta_{exp.} - \Delta_{calc.}}{\sigma_{\Delta_i}^{exp}} \right\}^2 \right] \quad (13)$$

in which  $\psi_{exp}$ ,  $\psi_{calc}$ , and  $\Delta_{exp}$ ,  $\Delta_{calc}$  are the measured and calculated ellipsometry functions respectively,  $N$  is the number of measured pairs ( $\psi$  and  $\Delta$ ),  $M$  is the number of fitted parameters in the model and  $\sigma$  is the standard deviation for each of the experimental data points.

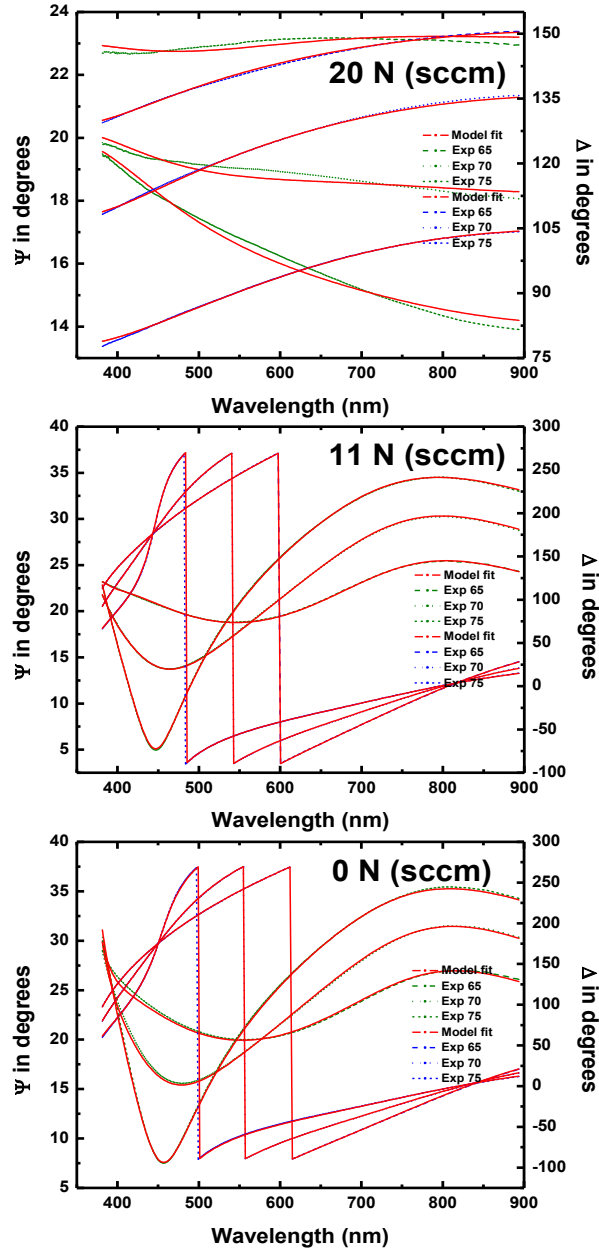


Figure 4.7: Spectral dependence of  $\psi$  and  $\Delta$  for W-O-N nano-coatings grown with varying nitrogen flow with experiment data and modeling curves shown.

Using the TL-oscillator, the best fit for the data was determined while maintaining the minimal MSE, the results of which are represented in Table 4.2.

Table 4.2: Tauc-Lorentz oscillator parameters used to fit the optical constants for W-O-N nano-coatings as a function of nitrogen flow rate.

$N_2$ flow rate (sccm)	MSE	Thickness (nm)	A	B	$E_0$ (eV)	$E_g$ (eV)
0	6.83	1040.65	54.25	0.04	4.09	2.99
3	5.88	1050.54	45.50	0.30	4.13	2.87
5	4.74	1029.61	32.86	0.45	4.33	2.57
7	2.06	1030.52	18.18	0.45	4.10	2.30
9	1.49	1032.61	15.22	0.66	4.15	2.10
11	1.53	987.31	17.03	1.15	4.25	2.05
13	1.80	1019.65	14.95	1.40	4.15	1.92
15	2.32	1024.23	23.23	2.09	4.13	1.94
17	5.39	978.97	40.51	2.86	3.97	1.89

Using the 4 unique parameters associated with the TL oscillator, amplitude ( $A$ ) of the  $\varepsilon_2$  peak, the half width ( $C$ ) of the  $\varepsilon_2$  peak, fixed center energy ( $E_0$ ) of the TL peak, and the Tauc gap ( $E_g$ ) it was possible to construct the variation of  $E_g$  as a function of nitrogen flow rate represented by Figure 4.8.

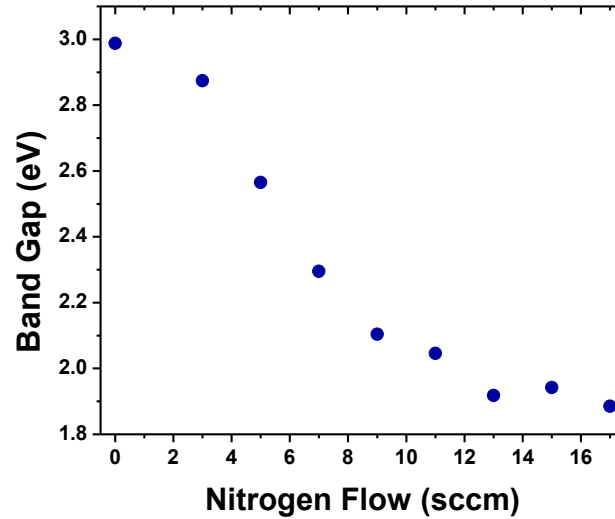


Figure 4.8: Band gap variation in W-O-N nano-coatings with varying nitrogen flow rate. The variation of  $E_g$  indicates a change in the electronic structure of the coatings as nitrogen is incorporated.

The  $E_g$  value of  $\sim 2.99 (\pm 3\%)$  eV for the W-O-N coating grown without any nitrogen matches with the values reported in the literature for  $\text{WO}_3$  films [5-10, 43, 47, 67] and the trend of decreasing band gap values with nitrogen incorporation has also been reported by several authors [10, 43-45]. This phenomenon can be attributed to both oxide and nitride like behavior having an influence on the band gap of the samples indicating a composite-like material. As noted by Mohamed et al., there is a transition from the insulating  $\text{WO}_3$  to the metallic  $\text{W}_2\text{N}$ . This is indicated by the fall in band gap values as nitrogen flow increases [44], as confirmed by compositional analysis indicating significant nitrogen incorporation at a nitrogen flow rate of 9 sccm. The same observation was made in tantalum oxynitrides [57] and titanium oxynitride [59] that also transitioned from the behavior of an oxide to that of a nitride. Le Dreo et al. explain that tantalum oxynitride acts as a composite material and as nitrogen or oxygen is substituted into the lattice it causes a change in the optical properties of the coating [55]. This evidence indicates that the W-O-N coatings grown exhibit a composite structure and simultaneous semiconducting behavior.

Also determined by modeling the SE data, were the optical constants associated with the W-O-N coatings. The refraction index ( $n$ ) and extinction coefficient ( $k$ ) both show favorable characteristics and each is shown at 550 and 623 nm as a function of nitrogen flow below. As seen in Figure 4.9, the values for  $k$  are near zero, with a slight increase at higher nitrogen flows, which indicates very low optical losses due to absorption. For the  $n$  values it can be seen that there is a systematic increase in values, especially at higher nitrogen flows, indicating the same transition from an insulating-to-semiconducting then semi-metallic behavior that can be attributed to the composite-like nature of the coatings as described before. Overall the values of  $n$  for the coatings grown without nitrogen correspond well with values gathered by other authors for  $\text{WO}_3$  [6, 69].

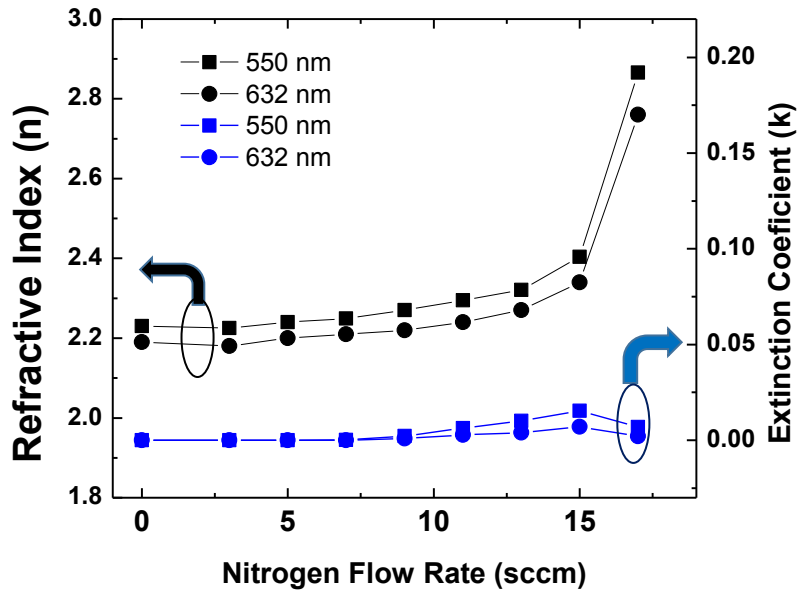


Figure 4.9: Refractive Index ( $n$ ) and Extinction Coefficient ( $k$ ) values at 550 and 632 nm, displayed as a function nitrogen flow

The dispersion profiles of the index of refraction ( $n$ ) are also displayed (Figure 4.10) and show a gradual increase in lower wavelengths. Of significance is the contrast in behavior of coatings with little or no nitrogen incorporation fabricated with nitrogen flow below 9 sccm (part a) versus those coatings with increasing nitrogen incorporation fabricated with nitrogen flows greater than 9 sccm (part b). W-O-N coatings show very similar values until nitrogen is incorporated into the coatings, causing an increase in values across all wavelengths and behavior more characteristic of metallic coatings at 17 sccm.

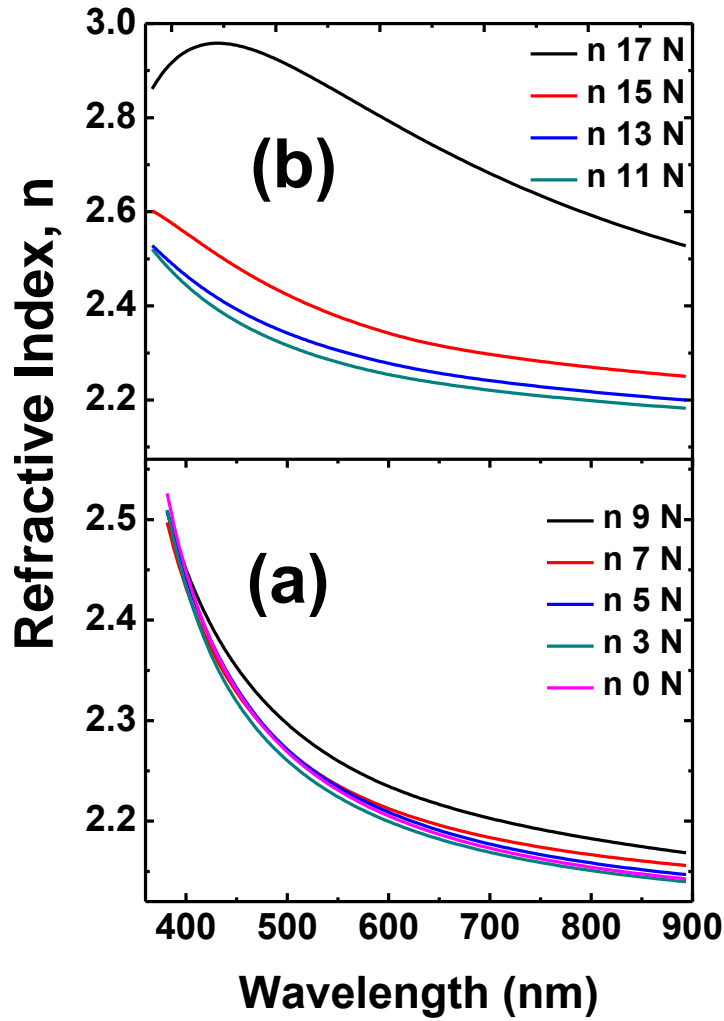


Figure 4.10: The dispersion profiles of index of refraction ( $n$ ) of W-O-N nano-coatings with little or no nitrogen incorporation (a) and increasing nitrogen incorporation (b)

Figure 4.11 presents the dispersion profiles of  $k(\lambda)$  for the coatings fabricated with little or no nitrogen incorporation (part a) and coatings with significant nitrogen incorporation (part b). As can be seen by the  $k(\lambda)$  curves, the coatings only display absorption in lower wavelengths and are smooth in behavior indicating the fabrication of high quality, highly transparent coatings. Both the dispersion profiles for  $n$  and  $k$  show an increase in values in all wavelengths as there is an increase in nitrogen incorporation, which follows similar observations by Mohammed et al. and Parreira et al. [44-46].

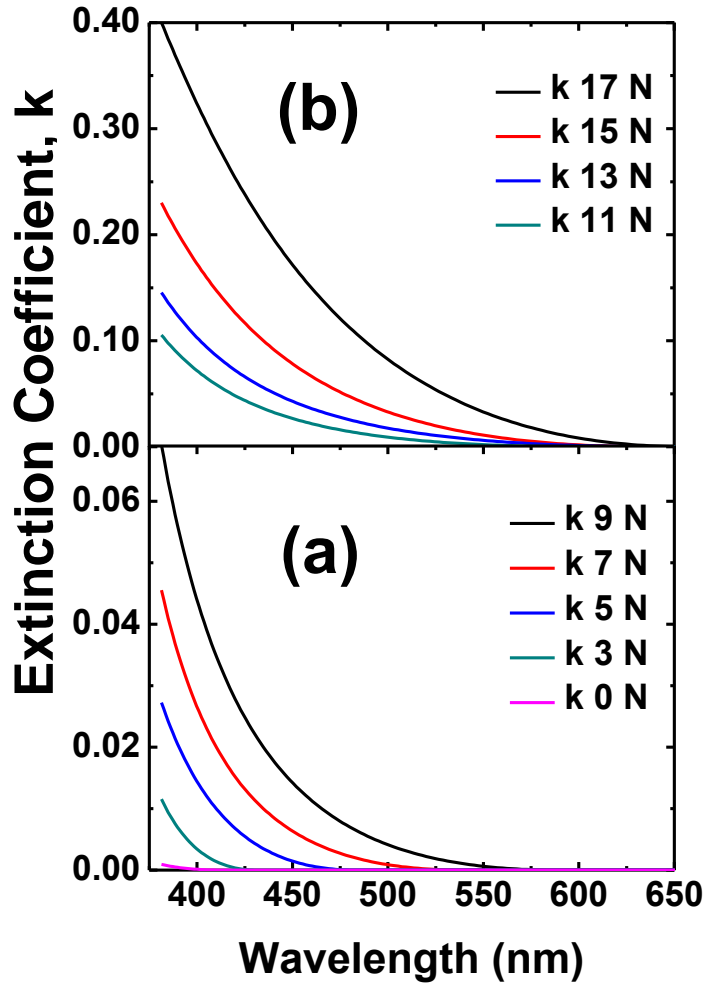


Figure 4.11:  $k(\lambda)$  curves of W-O-N nano-coatings with little or no nitrogen incorporation (a) and increasing nitrogen incorporation (b)

#### 4.4 MODELING THE OPTICAL DATA

Further analysis of the  $n$ -profiles and optical transmittance curves, as a function of nitrogen content, is made in order to confirm the optical behavior and to determine the energy dispersion parameters of the W-O-N coatings. First, the dispersion of the refractive index is simulated with the Wemple and DiDomenico (W-D) single-oscillator model to fit the energy dependence of the index of refraction ( $n$ ) using Equation 14:

$$n^2(E) - 1 = \frac{E_d E_0}{E_0^2 - E^2} \quad (14)$$

where  $E$  is the photon energy of the incident light,  $E_0$  is the oscillator energy and  $E_d$  is the dispersion energy [44-45, 76]. By plotting  $(n^2-1)^{-1}$  vs.  $E^2$  and fitting the relationship with a linear function, both  $E_0$  and  $E_d$  can be solved for by setting  $E_0/E_d$  equal to the y-intercept and  $-(E_0 E_d)^{-1}$  equal to the slope. An example of the method is presented in Figure 4.12 for the behavior of a sample deposited with a nitrogen flow of 9 sccm. When fitting a linear function to the plot it was seen that the data would only remain linear until the photon energy approached the band edge causing a deviance in the plot [76]. This observation resulted in the fitting of only the linear regions at low photon energies so as to obtain the most accurate modeling of the optical energies.

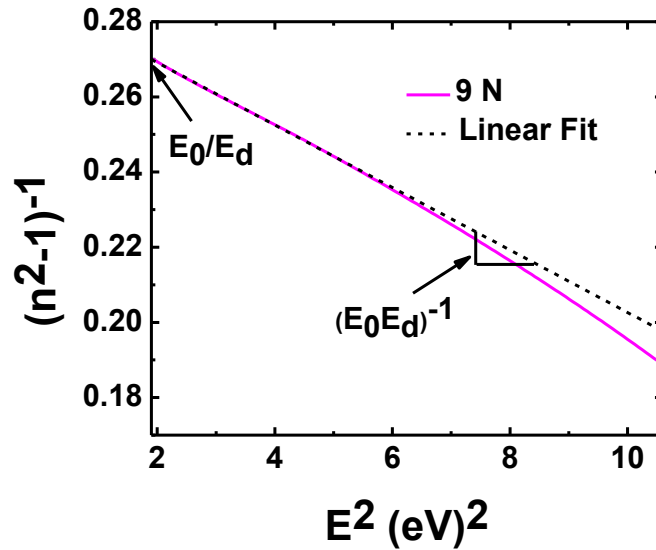


Figure 4.12: Singular  $(n^2-1)^{-1}$  vs.  $E^2$  plot, at 9 sccm nitrogen flow rate, fitted using a linear expression. In order to approximate the band gap using this method  $E_0$  and  $E_d$  must be calculated by setting  $E_0/E_d$  equal to the y-intercept and  $-(E_0 E_d)^{-1}$  equal to the slope.

The  $(n^2-1)^{-1}$  vs.  $E^2$  plots for all of the compositions of the W-O-N nano-coatings samples are displayed in Figure 4.13. It can be seen that all of the plots show sufficient linearity to

ensure accuracy of the data calculated using this method, interestingly a pattern in the deviation from linearity is also observed. It can be seen that two regions appear in the plots; the first region includes the plots with nitrogen flow rate from 0-9 sccm, indicating those samples with little or no nitrogen incorporation, with a negative curvature at higher energies and the second region shows a positive curvature at the same energies.

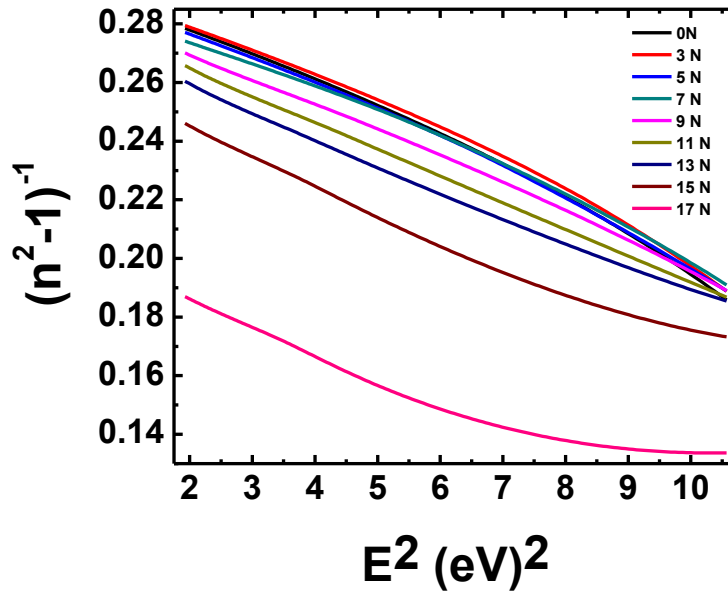


Figure 4.13:  $(n^2-1)^{-1}$  vs.  $E^2$  plots for the index of refractive ( $n$ ) fitted using the single-oscillator model

Overall the plots allowed for the calculation of accurate and dependable data, the results of which are shown in Table 4.3. Along with the oscillator energy ( $E_0$ ) and dispersion energy ( $E_d$ ), the band gap ( $E_g$ ) was also approximated using the relation  $2E_0 \approx E_g$  and are also displayed in Table 2 [44-45]. The  $E_g$  values approximated using this method are in agreement with the values calculated using the Tauc-Lorentz fitting of the raw SE data with values of  $\sim 3.0$  eV for samples with a  $\text{WO}_3$  composition and a drop in values to 2.289 eV for W-O-N samples with the highest amounts of nitrogen incorporation.

Table 4.3: Calculated values for  $E_g$ ,  $E_0$  and  $E_d$  as gathered by the single-oscillator method for fitting the index of refraction ( $n$ )

$N_2$ flow rate (sccm)	$E_g$ (eV)	$E_0$ (eV)	$E_d$ (eV)
0	2.912	5.825	19.689
3	2.978	5.957	20.129
5	2.945	5.889	20.047
7	3.085	6.170	21.326
9	2.932	5.864	20.521
11	2.789	5.579	19.741
13	2.716	5.431	19.547
15	2.537	5.074	19.097
17	2.289	4.578	22.243

Besides the approximated band gap values, the oscillator and dispersion energies also show interesting trends that can be seen in Figure 4.14. Both  $E_0$  and  $E_d$  decrease with in increased amount of nitrogen flow, this trend matches with the results of Mohamed et al. for  $E_0$  in magnitude and decreasing value, but the behavior of  $E_d$  is contrary to that seen previously [44-45]. This trend can be seen as in indication of an increased amount of disorder in the coating's structure as nitrogen flow rate is increased during deposition and nitrogen atoms displace oxygen atoms leaving voids in the lattice.

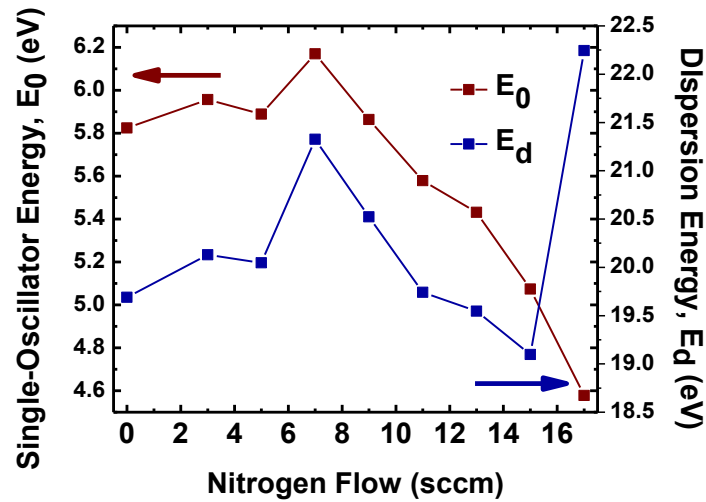


Figure 4.14:  $E_0$  and  $E_d$ , as calculated by fitting the index of refraction ( $n$ ) to the single-oscillator model, and as a function of the flow rate of nitrogen gas

This theory prompted further investigation into the dispersion energy, since this value is related to the chemical bonding within the coatings as a characteristic parameter that depends on charge distribution. The dispersion energy  $E_d$  is related to the coordination number and chemical valency of the coating through Equation 15 [44-45, 76];

$$E_d = \beta N_c Z_a N_e \quad (15)$$

where  $\beta$  is an ionic or covalent value constant ( $\beta_i = 0.26 \pm 0.03$  eV and  $\beta_c = 0.37 \pm 0.04$  eV, respectively),  $N_c$  is the effective coordination number of the cation (nearest the anion),  $Z_a$  is the chemical valency of the anion(s) and  $N_e$  is the number of valence electrons per anion(s). For  $\beta$  the ionic value was chosen due to the nature of W-O-N coatings, and  $Z_a$  and  $N_e$  were calculated using the coating's chemical composition as found by RBS, using W the cation and O and N as the anions in bonds formed in the coatings. In Figure 4.15,  $Z_a$  and  $N_e$  are displayed as a function of nitrogen gas flow, where opposite trend can be noted. The increase in  $Z_a$  and decrease in  $N_e$  are attributed to a valence electron shift in the coatings due to increased nitrogen incorporation.

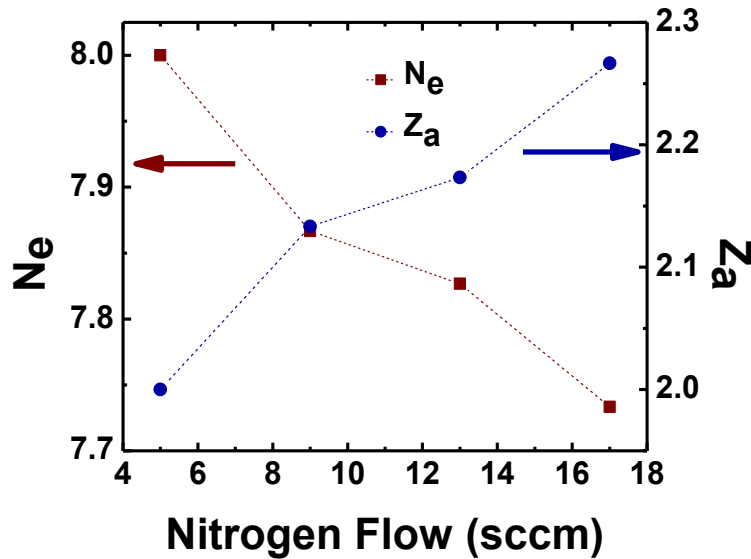


Figure 4.15:  $Z_a$  and  $N_e$  as calculated using the chemical composition of the W-O-N nano-coatings as calculated by RBS analysis

With these values, it is possible to find the effective coordination number of tungsten ( $N_c$ ) using the relation described above. The results of the analysis of  $E_d$ , along with results for the energies attributed to the single-oscillator model are shown in Table 4.4. It can be seen from viewing the results, that  $E_d$  can be directly attributed charge distribution and is closely related to the chemical bonding within the material. The behavior of  $E_d$  can then be said to be a result of increased disorder within the coatings, causing chemical bonding to be affected.

Table 4.4: The results of the complete analysis of the fitting of the refractive index ( $n$ ) to the single-oscillator model taking into account the chemical composition of the nano-coatings

<b>N<sub>2</sub> flow rate (sccm)</b>	<b>Composition</b>	<b>E<sub>g</sub> (eV)</b>	<b>E<sub>0</sub> (eV)</b>	<b>E<sub>d</sub> (eV)</b>	<b>Z<sub>a</sub></b>	<b>N<sub>e</sub></b>	<b>N<sub>c</sub></b>
5	WO <sub>3</sub>	2.945	5.889	20.047	2	8	4.819
9	WO <sub>2.60</sub> N <sub>0.40</sub>	2.932	5.864	20.521	2.133	7.867	4.703
13	WO <sub>2.48</sub> N <sub>0.52</sub>	2.716	5.431	19.547	2.173	7.827	4.420
17	WO <sub>2.20</sub> N <sub>0.80</sub>	2.289	4.578	22.243	2.267	7.733	4.881

Assuming that a transition exists between the edges of the valence and conduction bands, the Tauc-Relation can be used to analyze the transmittance data gathered by UV-VIS-NIR spectroscopy. The optical band gap  $E_g$  can then be calculated using the relations described in chapter 3. By using transmittance data to find the absorption coefficient, it is possible to find  $E_g$  by plotting  $(\alpha h\nu)^{1/2}$  vs.  $h\nu$  and extrapolating the linear region to  $h\nu = 0$  resulting in the value of the sample's optical band gap [43, 56-58, 67]. Figure 4.16 shows an example (9 sccm nitrogen flow) of this relation and how it was used to find the band gap for each sample indicated by the arrow.

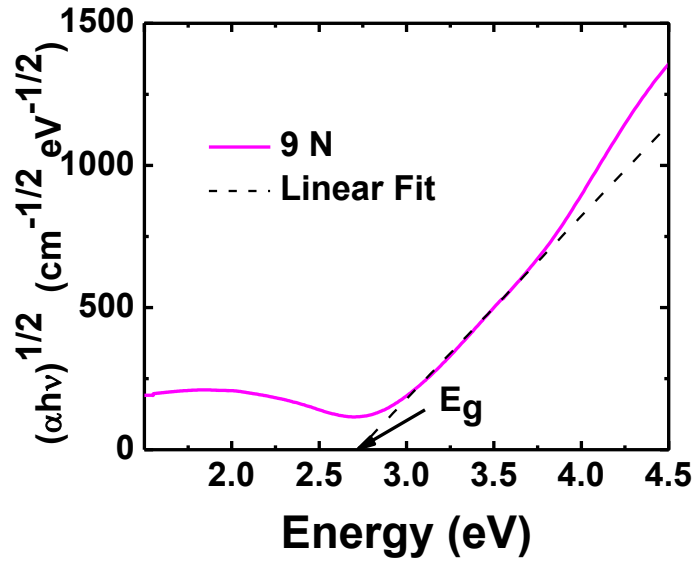


Figure 4.16:  $(\alpha h\nu)^{1/2}$  vs.  $h\nu$  plot for W-O-N nano-coatings deposited with 15 sccm of nitrogen. The linear region of the plot is extrapolated to  $h\nu = 0$  in order to calculate the value for  $E_g$

This method is then applied to all of the compositions of W-O-N (Figure 4.17) results of which show a gradual trend towards lower energies as the flow of nitrogen gas is increased.

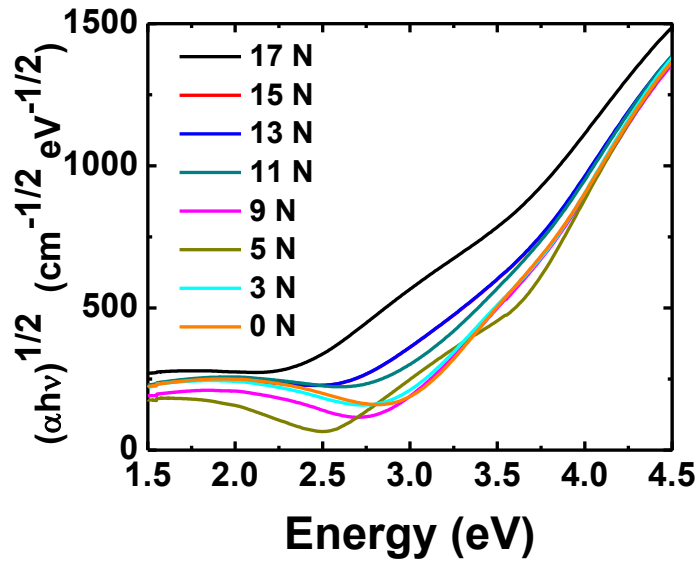


Figure 4.17:  $(\alpha h\nu)^{1/2}$  vs.  $h\nu$  plot for various W-O-N thin nano-coatings deposited increasing nitrogen gas flow rates

The results for  $E_g$  for both the Single-Oscillator model and Tauc-Relation are presented in Figure 4.18. Each set of data matches well in both magnitude and behavior as it relates to the flow of nitrogen gas. Using either method, there is an observed decrease in the optical band gap, from an initial value of  $\sim 3.0$  ( $\pm 0.09$ ) eV, as the nitrogen flow increases. Like the values determined by directly applying the raw SE data to the TL model, the initial values match well with previous values of  $\sim 2.99$  ( $\pm 3\%$ ) eV for  $\text{WO}_3$  films [5-10, 43, 47, 67] and decreasing values with increased nitrogen content match well with results of previous authors as well [10, 43-45].

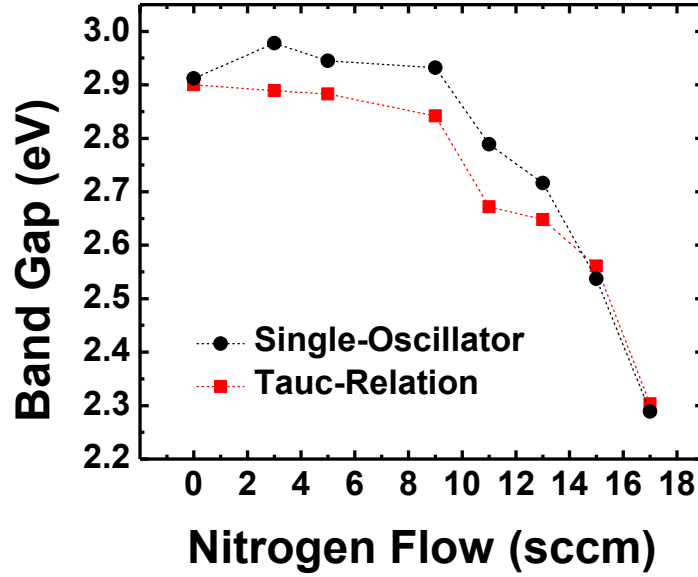


Figure 4.18: Optical band gap ( $E_g$ ) values as a function of nitrogen flow rate as determined by applying the Single-Oscillator model and Tauc Relation to the optical constants found by SE

#### 4.5 MECHANICAL PROPERTIES

The results of the nano-indentation testing are seen in Figure 4.19 in terms of both the nano-coating's hardness and Young's modulus. By using load control nano-indentation, the stiffness ( $S$ ) of each sample was determined from the slope of the unloading curve of the load vs. displacement graph of each coating. Since the geometry, and thus the area of contact ( $A$ ) at peak load, and mechanical properties of the indenter were known, the mechanical properties of the

coatings were calculated using the method described previously in a work authored by Oliver and Pharr and outlined in Methodology [68]. As can be seen in Figure 4.19, both the hardness and Young's modulus follow the same trajectory as one another and the same can be seen in the results given by Khamseh and Parreira et al. [46, 53]. Both the hardness and Young's modulus initially increase to maximum values of 4.46 GPa and 98.5 GPa, respectively, at a flow of 5 sccm then decrease from this point reaching minimum values of 3.57 GPa and 72.91 at a nitrogen flow rate of 15 sccm. This is only a fraction of the values found by previous authors whose values ranged between 15 and 30 GPa [46, 52-53], but the low values can be attributed to the amorphous structure of the nano-coatings, the substrate material used and a lower thickness characterized than previously investigated coatings [60, 77]. The decreasing trend seen in Figure 4.19 however, only exists commonly with samples characterized as having an increase of oxygen incorporation that contributes to a relaxation of internal stresses [46, 53]. This is not the case since all characterization of the W-O-N coatings indicate that the coating's mechanical properties are decreasing in value as there is an increase in nitrogen incorporation, especially after 9 sccm of nitrogen flow as evident by XPS and RBS analysis. These observations, however, indicate that the samples grown encounter a decrease in hardness and Young's modulus because of the competition between nitrogen and oxygen atoms to form bonds with tungsten, causing an increasingly amorphous surface. Evidence of this phenomenon can be seen in the earlier analysis done to determine the dispersion energy ( $E_d$ ) of the coatings which can help describe physical parameters of the material and chemical bonding [44, 76]. Seen in the dispersion energy is the same decreasing trend in value, which can signify an increase in the disorder of the atoms forming the bond of the W-O-N nano-coatings.

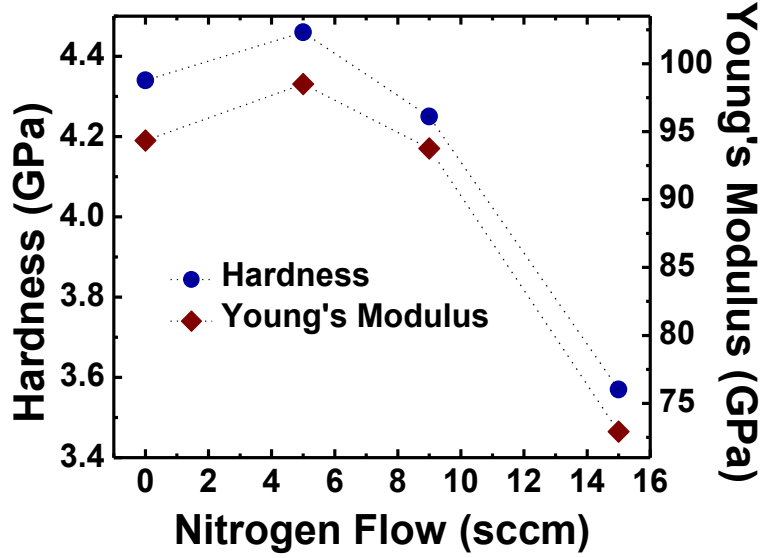


Figure 4.19: Mechanical properties, hardness and Young's modulus, of W-O-N nano-coatings represented as a function of nitrogen gas flow rate and measured by nano-indentation tests.

Optical properties were considered to model the physical density of the W-O-N coatings, accounting for the observed optical properties and to describe the physical significance of said properties. The densities of the W-O-N coatings were calculated using the Lorentz-Lorentz relation described in Equation 16 [6, 69]:

$$\frac{\rho_f}{\rho_b} = \left[ \frac{(n_f - 1)^2}{(n_f + 1)^2} \cdot \frac{(n_b + 1)^2}{(n_b - 1)^2} \right], \quad (16)$$

where  $\rho_f$  and  $\rho_d$  are the densities of the deposited coatings and bulk material, respectively,  $n_f$  is the refractive index for the W-O-N nano-coatings and  $n_b$  is the estimated refractive index for bulk W-O-N. The rule of mixtures was employed to calculate the bulk density. In order to estimate the density and index of refraction ( $n_b$ ) values for the bulk materials, the fraction of W-O and W-N bonds within  $\text{WO}_x\text{N}_y$  were calculated using the chemical composition found through XPS and RBS analysis. The fractions of each bond were then used to estimate the new value of the bulk material by assuming the index of refraction for bulk  $\text{WO}_3$  and  $\text{WN}$ , at  $\sim 633$  nm, to be 2.0 [78] and 3.8 [79-80], respectively, and the bulk densities to be  $7.16 \text{ g/cm}^3$  [16] and  $17.7 \text{ g/cm}^3$  [37],

respectfully. The measured values,  $n$ , at  $\sim 633$  nm from SE for W-O-N coatings were then used to calculate the approximate values of the density for the deposited W-O-N thin coatings as a function of nitrogen flow rate. The results of the analysis are presented in Figure 4.20 and it can be seen that there is a direct correlation between the measured index of refraction and density of the coatings. The index of refraction and density both increase as a direct consequence of increased nitrogen content in coatings with increasing nitrogen gas flow rate. Mohamed et al. theorizes that the index of refraction increases in films are due to increased density and molecular polarizability, thus providing a link between the physical characteristics of W-O-N and the optical properties [45].

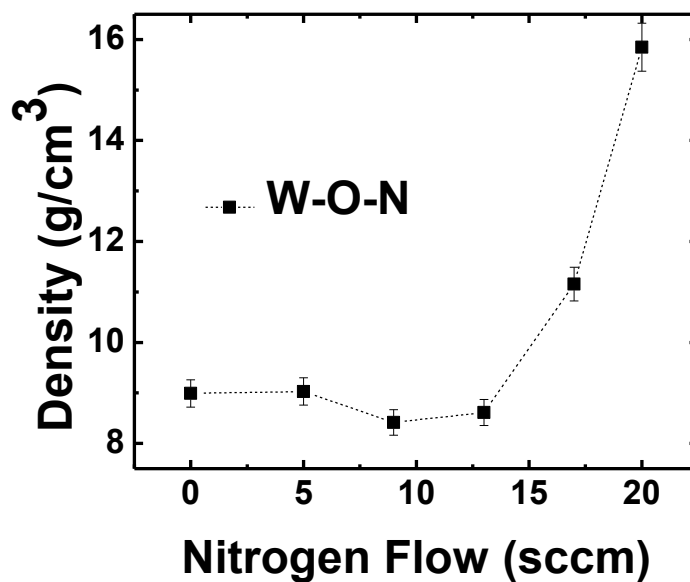


Figure 4.20: Density variation of W-O-N nano-coatings with nitrogen flow rate. It is evident that the coating's density increases with increasing nitrogen gas flow rate.

## Chapter 5: Physical, Mechanical, Chemical and Optical Property Correlation

The purpose of this chapter is to present a physical, mechanical, chemical and optical property correlation in amorphous W-O-N nano-coatings based on the results and discussion presented in chapter 4. Additional analysis and modeling of the data is presented if there is a further need to establish such a correlation between the processing conditions and properties.

In this work, most important observation is a decrease in band gap values with increasing nitrogen flow rate. Two separate regions of band gap values can be seen in the reported data; the first region including samples deposited with 0 to 9 sccm of nitrogen flow rate show values near that of stoichiometric  $\text{WO}_3$ , subsequent band gap values above 9 sccm show much lower values characteristic of tungsten nitrides. The shift in band gap values are thus a direct result of nitrogen incorporation taking place, subsequently increasing at nitrogen flow rates above 9 sccm, as indicated by XPS and RBS analysis. Even though direct comparison of nitrogen content and band gap values is not possible since both depend on processing conditions, it is possible to conclude that nitrogen content plays a major role. Similar trends have been reported by several authors, explaining that band gap values fall when there are increased amounts of nitrogen incorporation [6, 43-45]. There are two approaches at understanding the physics involved in this phenomenon, the first attributes the loss of band gap to a change in ionicity as nitrogen atoms are incorporated into the oxide lattice. Initially suggested by Futsuhara et al., the author bases the change in ionicity due to the incorporation of nitrogen atoms as the cause for the decreasing band gap values in zinc oxynitrides [54]. Since metal-oxygen (M-O) bonds have a higher ionicity than that of metal-nitrogen (M-N) bonds, because the electronegativity of oxygen is higher than that of nitrogen, a decrease in ionicity can be expected in samples with more nitrogen incorporation [43]. Thus with the increase of W-N bonds in the mixture of W-O and W-N in W-O-N coatings, the increased nitrogen content causes the observed band gap decrease. An additional explanation presented later for decreasing band gap values is the narrowing of the band gap due to the existence of both the N 2p states with O 2p states simultaneously [43-44].

Corresponding to the electronic transitions from the top of the valence band to the conduction band [5-8, 10, 43, 47, 60], band gap values in  $\text{WO}_3$  are formed by the transition from the valence band formed by the filled O 2p states and the conduction band formed by the empty W 5d states. The decrease in band gap values can then be said to be caused by nitrogen incorporation increasing the intermixing of N 2p states with O 2p states in the valence band [43-44]. The expansion of the valence band by N 2p states occupied above the O 2p states, results in lower band gap values. A representation of this phenomenon is presented in Figure 5.1 to schematically visualize the change in electronic transitions as nitrogen is incorporated into the coating. The higher values of  $E_g$  match the samples that are predominantly  $\text{WO}_3$  in composition, and the band gap corresponds to the energy gap between valence and conduction bands formed by O 2p and W 5d states, respectfully. Lower  $E_g$  values correspond to the electronic transitions from the valence band formed from a mixture of O 2p and N 2p states, formed as nitrogen is incorporated into the coating at 9 sccm of nitrogen flow rate and above. Such phenomena has been reported in past transition metal oxynitrides that act as a composite-like material, experiencing a transition from insulating M-O to semi-metallic M-N behavior [54-55, 57, 59].

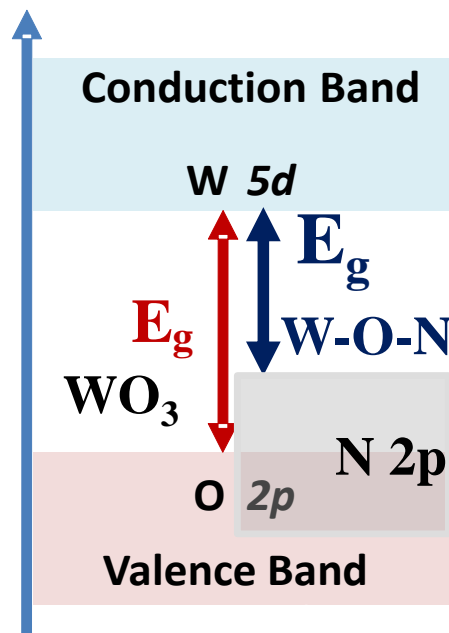


Figure 5.1: Proposed electronic structure model to account for the observed changes in the band gap of W-O-N nano-coatings. The variable, lower band gap in W-O-N corresponds to the electronic transitions from the new valence band, which is formed by a mixture of O 2p and N 2p states.

The optical constants  $n$  and  $k$  were also affected by the change in nitrogen incorporation. As can be seen in the dispersion profile of  $n$  in Figure 22, there is a clear distinction between  $n$  values above and below 9 sccm of nitrogen flow rate. Part a of Figure 22 shows the  $n$ -profile of those samples with  $\leq 9$  sccm nitrogen flow, and indicates the coatings are comprised of a W-oxide phase closely related to stoichiometry of  $\text{WO}_3$ . Above 9 sccm, it is observed that the magnitude of  $n$  increases, and a positive shift in  $n$ -profiles occurs as the amount of nitrogen content increases. At 17 sccm of nitrogen flow rate the  $n$ -profile demonstrates elevated values for  $n$ . The evolution of the  $n$ -profiles, indicated by Figure 22b, demonstrates that a composite of W-oxide and W-nitride is formed, leading to  $n$  values behaving in a manner resembling a hybrid of insulating  $\text{WO}_3$  and W-nitride. The increasing magnitude of both  $n$  and  $k$ , with increasing nitrogen content, is also indicative of the shift in electronic structure as a result of the coating's compositional change. This shift due to compositional changes is best represented by the change in density of the coatings. As a result of increasing nitrogen incorporation, the density, as calculated by the Lorentz-Lorentz relation, increases at values that correspond to the increase in the index of refraction since  $n$  values are known to be related to a material's density and/or molecular polarizability [45].

As further vindication of a shift in optical properties, the analysis done using the W-D single oscillator model indicated a dependence of optical dispersion on the chemical composition. Using this method, it was shown that the oscillator energy  $E_0$ , which simulates electronic excitations involved [76], shows a clear decreasing trend with increasing nitrogen flow. Band gap values estimated from  $E_0$  also show a clear trend and match well with band gap values calculated by other methods. More interesting are the values associated with the dispersion energy  $E_d$ , which measures the intensity of interband optical transitions [76]. The values for  $N_e$  and  $Z_a$  are calculated by the analysis of  $E_d$  which can help us further understand the

chemical bonding involved in the coating and the extent of charge transfer taking place to form such bonding. The increase in  $Z_a$  and corresponding decrease in  $N_e$  are a result of charge redistribution due to the increase in nitrogen content in the coatings. This redistribution is due to the same shift in ionicity described above and can also be related to values for  $E_0$  and  $E_g$  also gathered by this method. This analysis thus provides further proof that the optical properties depend heavily on the material's chemical composition.

As mentioned in the previous chapter, overall values for the mechanical properties, as tested by nano-indentation, were significantly lower than those values reported in the literature. This observation can be attributed to the coating's amorphous structure and the mechanical integrity of the substrate material. As indicated by the lack of crystalline formation across all nitrogen flow rates in the GIXRD results, the coatings formed are all amorphous in nature. Also, the coatings were grown on silicon substrates rather than substrates made of steel or a superalloy, which can lead to lower values in nano-indentation tests [77]. Widely accepted in the literature and reported by several authors, mechanical properties are demonstrated to decrease when films and coatings exhibit an amorphous structure and when the coating's internal stresses become relaxed [51, 53, 60]. As Dubey et al. demonstrated, binary and ternary nitrides differing in only structure will show a dependence on how well grain growth can provide a hindrance to dislocation movements [60]. Nitrides formed in face center cubic (FCC), hexagonal close pack (HCP) and amorphous structures showed the lowest values for mechanical properties in films with an amorphous structure, and this trend can be attributed to the increased degree in which the film is disordered.

Because of the observed change in chemical composition and chemical bonding, a shift in the mechanical behavior of the W-O-N coatings was expected with an increase in nitrogen content. A correlation can then be formed between the increasingly amorphous and disordered coatings and increasing nitrogen gas flow rate, due to the competitive nature of nitrogen and oxygen atoms during reactive deposition. Shen et al. reported that, with increasing oxygen concentration, there will be a competing tendency between nitrogen and oxygen atoms and the

relaxation of internal compressive stresses occur for either oxygen atoms taking the place of nitrogen atoms or nitrogen atoms substituting for oxygen within the lattice [49-50]. The decreasing hardness values then also lie in the fact that nitrogen incorporation is also known to hinder grain growth [50]. It has been demonstrated in studies of nitrides that nitrogen reduces the mobility of tungsten, or other metallic particles, or nitrogen can even act as a nucleation site for defects [38, 60]. These factors may lead to an increasingly amorphous structure, thus lower hardness and Young's modulus values, until enough nitrogen exist to begin to promote polycrystalline growth [38]. The drop in hardness and Young's modulus can then be understood as a relaxation of internal compressive stresses due to an increase in the disorder of the coating as indicated by the dispersion energy, representing the disorder term, as calculated by optical analysis. To demonstrate the relationship between the mechanical and optical properties of W-O-N coatings, Figure 5.2 shows the comparison in trends between the hardness, cation coordination number and density of the coatings. As a drop in the mechanical values occurs, there is a simultaneous decrease in the cation coordination number ( $N_c$ ), as calculated from the dispersion energy, and stagnation in density values. This indicates that before the density and cation coordination number of the coatings increase with higher nitrogen contents, the disorder of the coatings is increased due to vacancies in the lattice being formed by the substitution of oxygen by nitrogen atoms in the W-oxide lattice. This increased disorder hinders the coating's ability to counter dislocation movements, thus resulting in decreased mechanical properties as nitrogen content increases.

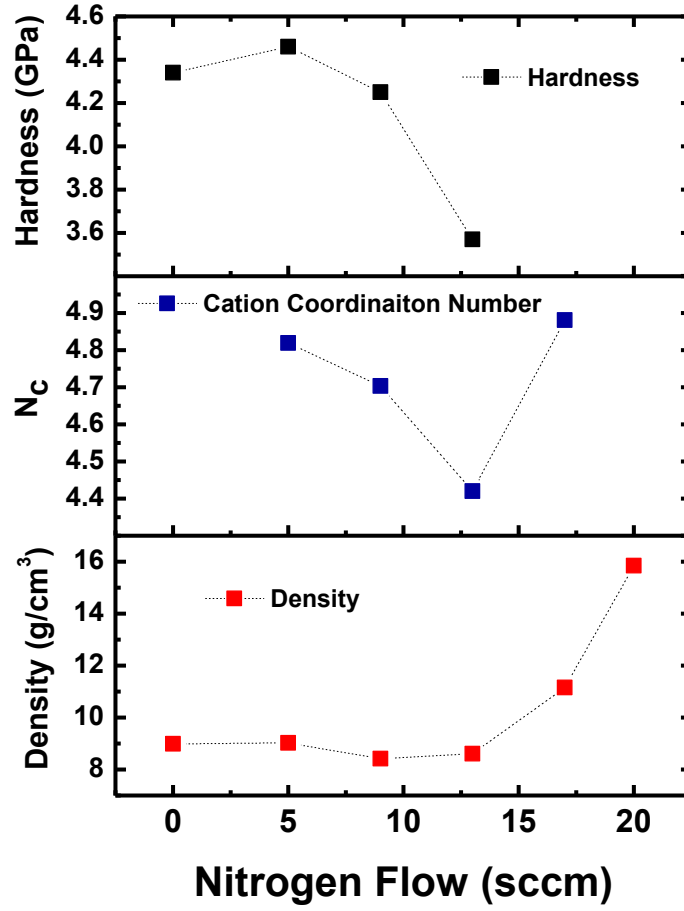


Figure 5.2: The hardness, cation coordination number ( $N_c$ ) and density of W-O-N coatings as a function of nitrogen flow rate. A direct relation between the mechanical properties (hardness) and physical properties ( $N_c$  and Density) determined from optical properties is apparent in this comparison.

Finally, optical properties were considered to model the physical density of the W-O-N coatings, accounting for the observed optical properties and to describe the physical significance of said properties. The densities of the W-O-N coatings were calculated using the Lorentz-Lorentz relation described in Equation 17 [6, 69]:

$$\frac{\rho_f}{\rho_b} = \left[ \frac{(n_f - 1)^2}{(n_f + 1)^2} \cdot \frac{(n_b + 1)^2}{(n_b - 1)^2} \right], \quad (17)$$

where  $\rho_f$  and  $\rho_d$  are the densities of the deposited coatings and bulk material, respectively,  $n_f$  is the refractive index for the W-O-N nano-coatings and  $n_b$  is the estimated refractive index for bulk W-O-N. The rule of mixtures was employed to calculate the bulk density. In order to estimate the density and index of refraction ( $n_b$ ) values for the bulk materials, the fraction of W-O and W-N bonds within  $WO_xN_y$  were calculated using the chemical composition found through XPS and RBS analysis. The fractions of each bond were then used to estimate the new value of the bulk material by assuming the index of refraction for bulk  $WO_3$  and  $WN$ , at  $\sim 633$  nm, to be 2.0 [78] and 3.8 [79-80], respectively, and the bulk densities to be  $7.16 \text{ g/cm}^3$  [16] and  $17.7 \text{ g/cm}^3$  [37], respectively. The measured values,  $n$ , at  $\sim 633$  nm from SE for W-O-N coatings were then used to calculate the approximate values of the density for the deposited W-O-N thin coatings as a function of nitrogen flow rate. The results of the analysis are presented in Figure 5.3 and it can be seen that there is a direct correlation between the measured index of refraction and density of the coatings.

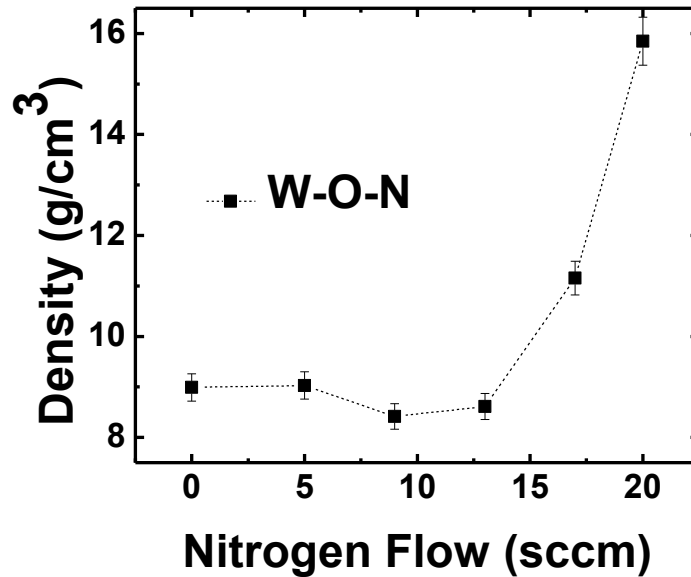


Figure 5.3: Density variation of W-O-N nano-coatings with nitrogen flow rate. It is evident that the coating's density increases with increasing nitrogen gas flow rate.

The index of refraction and density both increase as a direct consequence of increased nitrogen content in coatings with increasing nitrogen gas flow rate. Mohamed et al. theorizes that the index of refraction increases in films are due to increased density and molecular polarizability, thus providing a link between the physical characteristics of W-O-N and the optical properties [45]. Based on the observed results, discussion, analysis, and modelling of the data, the following correlation between electron structure, chemical composition, and physical properties (density) is proposed.

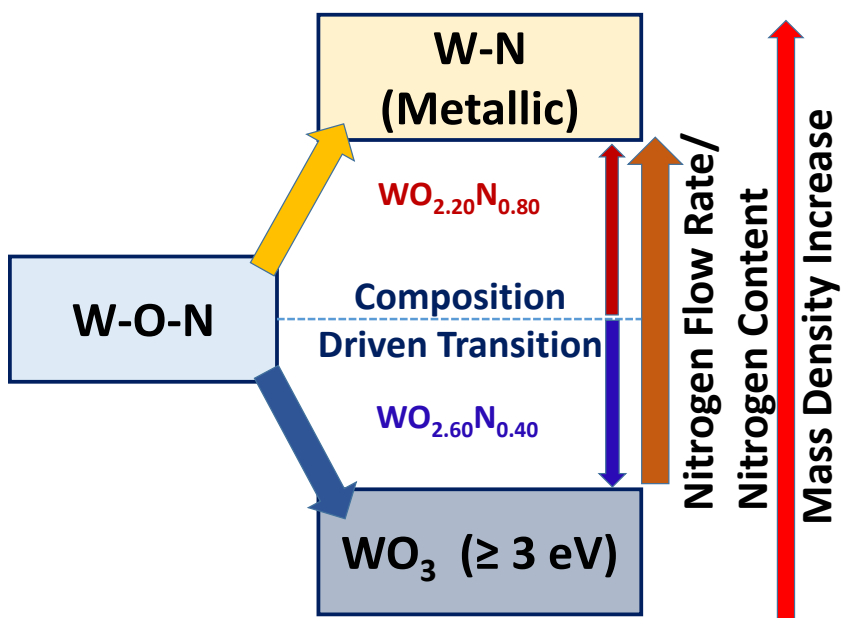


Figure 5.4: Proposed correlation between physical properties (density), chemistry (composition), and electronic structure (optical properties) of W-O-N nano-coatings.

## Chapter 6: Conclusions

Amorphous tungsten oxynitride nano-coatings were fabricated with varying nitrogen gas flow rate. The effect of chemical composition on the optical and mechanical properties is studied in detail. XPS and RBS analysis both demonstrate that no significant nitrogen incorporation takes place until 9 sccm of nitrogen flow rate. Optical analysis demonstrated the coating's optical properties strong dependence on nitrogen content. Optical transmittance spectra illustrated a red shift in the absorption and an overall decrease in transmission with increased nitrogen content. Further analysis of data gathered by SE by application of the TL model demonstrated an alteration in band gap ( $E_g$ ) values, showing a decrease in magnitude from values close to those reported for  $\text{WO}_3$  (~2.99 eV) to values resembling W-nitrides (~1.89 eV). Application of the Tauc-Relation and W-D single oscillator model further demonstrated a decrease in  $E_g$  values as the nitrogen content within the coatings increased and overall similar magnitudes, as found by the application of the TL model. Other optical properties affected by the change in chemical composition were the refractive index ( $n$ ) and the extinction coefficient ( $k$ ); both values increasing with the nitrogen content. The shift in both  $E_g$  and  $n$  values was a direct result of the formation a composite-like material with the intermixing of W-N bonds and W-O bonds significantly influencing optical properties.

The W-D single oscillator model also provided insight into the chemical bonding of the coating. The dispersion energy shows a decreasing trend in values as a function of nitrogen flow rate and signifies an increase in the disorder of the coatings. The optical disorder, consistency of the physical density in lower nitrogen flow rates and the competitive nature of nitrogen and oxygen atoms during deposition all account for the decreasing values for the mechanical properties as nitrogen gas flow is increased. By connecting these properties to the mechanical characterization, it is possible to form a relation between the optical and mechanical properties. Nano-indentation experiments yielded maximum values of 4.46 GPa and 98.5 GPa for hardness and Young's modulus, respectfully. These values were significantly lower than those reported in

the literature, but the lower values can be attributed to the lack of mechanical integrity of the substrates and amorphous structure of the coatings, regardless of nitrogen incorporation. A correlation between processing conditions, nitrogen chemistry, physical properties, electronic structure, optical constants and mechanical properties of amorphous W-O-N nano-coatings is established. Such a correlation derived in this study could provide a road-map to optimize the conditions to produce W-O-N coatings with enhanced performance in a given technological application.

## **Chapter 7: Future Work**

To further provide a complete characterization and analysis of W-O-N nano-coatings, it is required to pursue a more complete understanding of the key factors to tuning optical and mechanical properties.

1. Investigate the effect of thermal treatment on the structural, compositional, optical and mechanical properties.
2. Perform thermal treatment in both an Ar atmosphere and in the presence of oxygen in order to investigate any advantage either method can have on the optical and mechanical properties.
3. Perform thermal treatment at varying temperatures to investigate what thermal energy input can induce changes in optical and mechanical properties and to what extent.
4. Perform thermal treatment with the goal of forming a crystalline structure in the coating, in order to improve mechanical behavior.
5. Apply numerical analysis with software that forms relations between all of inputted empirical data.
6. Numerical modeling can provide direct formation of relations otherwise previously unknown, connecting physical, optical and mechanical properties of W-O-N nano-coatings

## References

1. C.G. Granqvist, Electrochromic materials: Microstructure, electronic bands, and optical properties, *Appl. Phys. A*. 57 (1993) 3–12.
2. S. Lee, H.M. Cheong, C.E. Tracy, A. Mascarenhas, A.W. Czanderna, S.K. Deb, Electrochromic coloration efficiency of  $\alpha$ -WO<sub>3-y</sub> thin films as a function of oxygen deficiency, *Appl. Phys. Lett.* 75 (1999) 1541–1543.
3. K. Nakagawa, N. Miura, S. Matsumoto, R. Nakano, H. Matsumoto, Electrochromism and Electronic Structures of Nitrogen Doped Tungsten Oxide Thin Films Prepared by RF Reactive Sputtering, *Jpn. J. Appl. Phys.* 47 (2008) 7230–7235.
4. K.R. Reyes-Gil, Z.D. Stephens, V. Stavila, D.B. Robinson, Composite WO<sub>3</sub>/TiO<sub>2</sub> Nanostructures for High Electrochromic Activity, *ACS Appl. Mater. Interfaces*. 7 (2015) 2202–2213.
5. H. Simchi, B.E. McCandless, T. Meng, W.N. Shafarman, Structural, optical, and surface properties of WO<sub>3</sub> thin films for solar cells, *J. Alloys Compd.* 617 (2014) 609–615.
6. C. V. Ramana, G. Baghmar, E.J. Rubio, M.J. Hernandez, Optical constants of amorphous, transparent titanium-doped tungsten oxide thin films, *ACS Appl. Mater. Interfaces*. 5 (2013) 4659–4666.
7. W. Li, P. Da, Y. Zhang, Y. Wang, X. Lin, X. Gong, G. Zheng, WO<sub>3</sub> nanoflakes for enhanced photoelectrochemical Conversion, *ACS Nano*. 8 (2014) 11770–11777.
8. S. Higashimoto, M. Sakiyama, M. Azuma, Photoelectrochemical properties of hybrid WO<sub>3</sub>/TiO<sub>2</sub> electrode- Effect of structures of WO<sub>3</sub> on charge separation behavior, *Thin Solid Films*. 503 (2006) 201–206.
9. A. Karuppasamy, A. Subrahmanyam, Studies on electrochromic smart windows based on titanium doped WO<sub>3</sub> thin films, *Thin Solid Films*. 516 (2007) 175–178.
10. A.K. Chawla, S. Singhal, H. Om Gupta, R. Chandra, Influence of nitrogen doping on the sputter-deposited WO<sub>3</sub> films, *Thin Solid Films*. 518 (2009) 1430–1433.
11. E.K.H. Salje, S. Rehmann, F. Pobell, D. Morris, K.S. Knight, T. Hermannsdorfer, M.T. Dove, Crystal structure and paramagnetic behavior of  $\epsilon$ -WO<sub>3-x</sub>, *J. Phys. Condens. Matter*. 9 (1997) 6563–6577.
12. M. Boulova, G. Lucazeau, Crystallite Nanosize Effect on the Structural Transitions of WO<sub>3</sub> Studied by Raman Spectroscopy, *J. Solid State Chem.* 167 (2002) 425–434.
13. M.B. Johansson, G. Baldissera, I. Valyukh, C. Persson, H. Arwin, G.A. Niklasson, L. Osterlund, Electronic and optical properties of nanocrystalline WO<sub>3</sub> thin films studied by optical spectroscopy and density functional calculations., *J. Phys. Condens. Matter*. 25 (2013) 205502.
14. N.M.G. Parreira, N.J.M. Carvalho, A. Cavaleiro, Synthesis, structural and mechanical characterization of sputtered tungsten oxide coatings, *Thin Solid Films*. 510 (2006) 191–196.
15. T. Polcar, N.M.G. Parreira, A. Cavaleiro, Tungsten oxide with different oxygen contents: Sliding properties, *Vacuum*. 81 (2007) 1426–1429.

16. T. Polcar, A. Cavaleiro, Structure, mechanical properties and tribology of W–N and W–O coatings, *Int. J. Refract. Met. Hard Mater.* 28 (2010) 15–22.
17. M. Uekubo, T. Oku, K. Nii, M. Murakami, K. Takahiro, S. Yamaguchi, T. Nakano, T. Ohta,  $WN_x$  diffusion barriers between Si and Cu, *Thin Solid Films*. 286 (1996) 170–175.
18. H.P. Kattelus, E. Kolawa, K. Affolter, M.-A. Nicolet, Sputtered W-N diffusion barriers, *J. Vac. Sci. Technol. A*. 3 (1985) 2246–2254.
19. F.C.T. So, E. Kolawa, X.-A. Zhao, E.T.-S. Pan, M.-A. Nicolet,  $W_xN_{1-x}$  alloys as diffusion barriers between Al and Si, *J. Appl. Phys.* 64 (1988) 2787.
20. Q.T. Vu, P.J. Pokela, C.L. Garden, E. Kolawa, S. Raud, M.-A. Nicolet, Thermal oxidation of reactively sputtered amorphous W80N20 films, *J. Appl. Phys.* 68 (1990) 6420–6423.
21. M. Takeyama, A. Noya, Preparation of  $WN_x$  films and their diffusion barrier properties in Cu/Si contact systems, *Japanese J. Appl. Phys.* 36 (1997) 2261–2266.
22. S. Bystrova, a. a. I. Aarnink, J. Holleman, R. a. M. Wolters, Atomic Layer Deposition of  $W_{1.5}N$  Barrier Films for Cu Metallization, *J. Electrochem. Soc.* 152 (2005) G522–G527.
23. M.H. Tsai, S.C. Sun, H.T. Chiu, S.H. Chuang, Metalorganic chemical vapor deposition of tungsten nitride for advanced metallization, *Appl. Phys. Lett.* 68 (1996) 1412–1414.
24. K.C. Hang, I.D. Eng, T.Y. Eh, K.L. Ain, Thermal Stability of Amorphous-like  $WN_x/W$  Bilayered Diffusion Barrier for Chemical Vapor Deposited-Tungsten/ $p^+$ -Si Contact System, *Jpn. J. Appl. Phys.* 38 (1999) 1343–1351.
25. L. Boukhris, J.-M. Poitevin, Electrical resistivity, structure and composition of d.c. sputtered  $WN_x$  films, *Thin Solid Films*. 310 (1997) 222–227.
26. B. Claflin, M. Binger, G. Lucovsky, Interface studies of tungsten nitride and titanium nitride composite metal gate electrodes with thin dielectric layers, *J. Vac. Sci. Technol.* 16 (1998) 1757–1761.
27. M. Moriwaki, T. Yamada, Y. Harada, S. Fujii, M. Yamanaka, J. Shibata, et al., Improved metal gate process by simultaneous gate-oxide nitridation during W/ $WN_x$  gate formation, *Jpn. J. Appl. Phys.* 39 (2000) 2177–2180.
28. J.W. Lee, C.H. Han, J.-S. Park, J.W. Park, Electrical characteristics and thermal stability of W,  $WN_x$ , and TiN Barriers in metal/ $Ta_2O_5$ /Si gate devices, *J. Electrochem. Soc.* 148 (2001) G95–G98.
29. P.-C. Jiang, J.S. Chen, Effects of Post-Metal Annealing on Electrical Characteristics and Thermal Stability of  $W_2N/Ta_2O_5/Si$  MOS Capacitors, *J. Electrochem. Soc.* 151 (2004) G751–G755.
30. P.-C. Jiang, Y.-S. Lai, J.S. Chen, Dependence of crystal structure and work function of  $WN_x$  films on the nitrogen content, *Appl. Phys. Lett.* 89 (2006) 122107.
31. T. Yamamoto, M. Kawate, H. Hasegawa, T. Suzuki, Effects of nitrogen concentration on microstructures of  $WN_x$  films synthesized by cathodic arc method, *Surf. Coatings Technol.* 193 (2005) 372–374.
32. T. Polcar, N.M.G. Parreira, A. Cavaleiro, Tribological characterization of tungsten nitride coatings deposited by reactive magnetron sputtering, *Wear*. 262 (2007) 655–665.

33. E.C. Samano, A. Clemente, J.A. Díaz, G. Soto, Mechanical properties optimization of tungsten nitride thin films grown by reactive sputtering and laser ablation, *Vacuum*. 85 (2010) 69–77.
34. T. Polcar, N.M.G. Parreira, A. Cavaleiro, Structural and tribological characterization of tungsten nitride coatings at elevated temperature, *Wear*. 265 (2008) 319–326.
35. I.N. Martev, D. a Dechev, N.P. Ivanov, T.D. Uzunov, E.P. Kashchieva, Characterization and properties of highly adhesive titanium nitride and tungsten nitride thin films, *J. Phys. Conf. Ser.* 113 (2008) 012025.
36. C.W. Lee, Y.T. Kim, High temperature thermal stability of plasma-deposited tungsten nitride Schottky contacts to GaAs, *Solid State Electron*. 38 (1995) 679–682.
37. Y.G. Shen, Y.W. Mai, Effect of deposition conditions on internal stresses and microstructure of reactively sputtered tungsten nitride films, *Surf. Coatings Technol.* 127 (2000) 239–246.
38. Y.G. Shen, Y.W. Mai, D.R. McKenzie, Q.C. Zhang, W.D. McFall, W.E. McBride, Composition, residual stress, and structural properties of thin tungsten nitride films deposited by reactive magnetron sputtering, *J. Appl. Phys.* 88 (2000) 1380-1388.
39. Y.G. Shen, Y.W. Mai, Microstructure and structure characteristics of cubic  $WN_x$  compounds, *Mater. Sci. Eng. A*. 288 (2000) 47–53.
40. M. Wen, Q.N. Meng, W.X. Yu, W.T. Zheng, S.X. Mao, M.J. Hua, Growth, stress and hardness of reactively sputtered tungsten nitride thin films, *Surf. Coatings Technol.* 205 (2010) 1953–1961.
41. M.T. Hosseinnajad, M. Ghoranneviss, G.R. Etaati, M. Shirazi, Z. Ghorannevis, Deposition of tungsten nitride thin films by plasma focus device at different axial and angular positions, *Appl. Surf. Sci.* 257 (2011) 7653–7658.
42. S. Khamseh, A study of the oxidation behavior of multilayered tungsten nitride/amorphous tungsten oxide film prepared in a planar magnetron sputtering system, *Ceram. Int.* 40 (2014) 465–470.
43. S.H. Mohamed, A. Anders, Structural, optical, and electrical properties of  $WO_x(N_y)$  films deposited by reactive dual magnetron sputtering, *Surf. Coatings Technol.* 201 (2006) 2977–2983.
44. S.H. Mohamed, A. Anders, I. Montero, L. Galán, Structural and optical evaluation of  $WO_xN_y$  films deposited by reactive magnetron sputtering, *J. Phys. Chem. Solids*. 68 (2007) 2227–2232.
45. S.H. Mohamed, E.R. Shaaban, Investigation of the refractive index and dispersion parameters of tungsten oxynitride thin films, *Mater. Chem. Phys.* 121 (2010) 249–253.
46. N.M.G. Parreira, T. Polcar, N. Martin, O. Banakh, A. Cavaleiro, Optical and Electrical Properties of W-O-N Coatings Deposited by DC Reactive Sputtering, *Plasma Process. Polym.* 4 (2007) S69–S75.
47. X. Sun, Z. Liu, H. Cao, Electrochromic properties of N-doped tungsten oxide thin films prepared by reactive DC-pulsed sputtering, *Thin Solid Films*. 519 (2011) 3032–3036.

48. R.S. Vemuri, M. Noor-A-Alam, S.K. Gullapalli, M.H. Engelhard, C.V. Ramana, Nitrogen-incorporation induced changes in the microstructure of nanocrystalline  $\text{WO}_3$  thin films, *Thin Solid Films*. 520 (2011) 1446–1450.
49. Y.G. Shen, Y.W. Mai, Effect of oxygen on residual stress and structural properties of tungsten nitride films grown by reactive magnetron sputtering, *Mater. Sci. Eng. B*. 76 (2000) 107–115.
50. Y.G. Shen, Y.W. Mai, Reactively sputtered  $\text{WO}_x\text{N}_y$  films, *J. Mater. Res.* 15 (2000) 2437–2445.
51. N.M.G. Parreira, N.J.M. Carvalho, F. Vaz, A. Cavaleiro, Mechanical evaluation of unbiased W–O–N coatings deposited by d.c. reactive magnetron sputtering, *Surf. Coatings Technol.* 200 (2006) 6511–6516.
52. C. Louro, J.C. Oliveira, A. Cavaleiro, Effects of O addition on the thermal behaviour of hard W–N sputtered coatings, *Vacuum*. 83 (2009) 1224–1227.
53. S. Khamseh, Synthesis and characterization of tungsten oxynitride films deposited by reactive magnetron sputtering, *J. Alloys Compd.* 611 (2014) 249–252.
54. M. Futsuhara, K. Yoshioka, O. Takai, Optical properties of zinc oxynitride thin films, *Thin Solid Films*. 317 (1998) 322–325.
55. H. Le Dréo, O. Banakh, H. Keppner, P.-A. Steinmann, D. Briand, N.F. de Rooij, Optical, electrical and mechanical properties of the tantalum oxynitride thin films deposited by pulsing reactive gas sputtering, *Thin Solid Films*. 515 (2006) 952–956.
56. S.K. Rawal, A.K. Chawla, V. Chawla, R. Jayaganthan, R. Chandra, Structural, optical and hydrophobic properties of sputter deposited zirconium oxynitride films, *Mater. Sci. Eng. B*. 172 (2010) 259–266.
57. J.P. Zhang, L.D. Zhang, L.Q. Zhu, Y. Zhang, M. Liu, X.J. Wang, et al., Characterization of  $\text{ZnO:N}$  films prepared by annealing sputtered zinc oxynitride films at different temperatures, *J. Appl. Phys.* 102 (2007) 114903.
58. J.H. Hsieh, C.C. Chang, J.S. Cherng, F.Y. Hsu, Optical properties and hydrophilic behaviors of  $\text{TaO}_x\text{N}_y$  thin films with and without rapid thermal annealing, *Thin Solid Films*. 517 (2009) 4711–4714.
59. X. Yang, C. Li, B. Yang, W. Wang, Y. Qian, Optical properties of titanium oxynitride nanocrystals synthesized via a thermal liquid-solid metathesis reaction, *Chem. Phys. Lett.* 383 (2004) 502–506.
60. P. Dubey, V. Arya, S. Srivastava, D. Singh, R. Chandra, Effect of nitrogen flow rate on structural and mechanical properties of Zirconium Tungsten Nitride (Zr–W–N) coatings deposited by magnetron sputtering, *Surf. Coatings Technol.* 236 (2013) 182–187.
61. P. Dubey, V. Dave, S. Srivastava, D. Singh, R. Chandra, Study of thermal stability and mechanical properties of amorphous  $\text{Zr}_{19}\text{W}_{18}\text{N}_{63}$  coatings deposited by DC/RF reactive magnetron sputtering, *Surf. Coatings Technol.* 237 (2013) 205–211.
62. P.J. Martin, Review Ion-based methods for optical thin film deposition, *J. Mater. Sci.* 21 (1986) 1–25.

63. K. Seshan, ed., Handbook of Thin-Film Deposition Processes and Techniques, 2002.
64. I.P. Jain, G. Agarwal, Ion beam induced surface and interface engineering, *Surf. Sci. Rep.* 66 (2011) 77–172.
65. SIMNRA is a Microsoft Windows program for the simulation of backscattering spectra for ion beam analysis with MeV ions. Additional details can be found in: Mayer, M. *SIMNRA User's Guide, Technical Report IPP 9/113*, Max-Planck-Institut für Plasmaphysik, Garching, Germany, (1997).
66. S.S. Kumar, E.J. Rubio, M. Noor-A-Alam, G. Martinez, S. Manandhar, V. Shutthanandan, S. Thevuthasan, C.V. Ramana, Structure, morphology, and optical properties of amorphous and nanocrystalline gallium oxide thin films, *J. Phys. Chem. C* 117 (2013) 4194–4200.
67. S.K. Gullapalli, R.S. Vemuri, C.V. Ramana, Structural transformation induced changes in the optical properties of nanocrystalline tungsten oxide thin films, *Appl. Phys. Lett.* 96 (2010) 171903.
68. W.C. Oliver, G.M. Pharr, An improved technique for determining hardness and elastic modulus using load and displacement sensing indentation experiments, *J. Mater. Res.* 7 (1992) 1564–1583.
69. M. Vargas, E.J. Rubio, A. Gutierrez, C.V. Ramana, Spectroscopic ellipsometry determination of the optical constants of titanium-doped WO<sub>3</sub> films made by co-sputter deposition, *J. Appl. Phys.* 115 (2014) 133511.
70. J. Tauc, R. Grigorovici, A. Vancu, Optical properties and electronic structure of amorphous Germanium, *Phys. Stat. Sol. B* 15 (1966) 627–637.
71. G.E. Jellison, Jr, Spectroscopic ellipsometry data analysis: measured versus calculated quantities, *Thin Solid Films* 313–314 (1998) 33–39.
72. H. Fujiwara, *Spectroscopic Ellipsometry: Principles and Applications*, John Wiley & Sons Inc, (2007).
73. J. A. Woollam Co., Inc., *Guide to Using WVASE32 Spectroscopic Ellipsometry Data Acquisition and Analysis Software* (2008).
74. P.I. Rovira, R.W. Collins, Analysis of specular and textured SnO<sub>2</sub>:F films by high speed four-parameter Stokes vector spectroscopy, *J. Appl. Phys.* 85 (1999) 2015.
75. H. Fujiwara, M. Kondo, Effects of carrier concentration on the dielectric function of ZnO:Ga and In<sub>2</sub>O<sub>3</sub>:Sn studied by spectroscopic ellipsometry: Analysis of free-carrier and band-edge absorption, *Phys. Rev. B* 71 (2005) 075109.
76. S.H. Wemple, M. DiDomenico, Behavior of the electronic dielectric constant in covalent and ionic materials, *Phys. Rev. B* 3 (1971) 1338–1351.
77. R. Saha, W.D. Nix, Effects of the substrate on the determination of thin film mechanical properties by nanoindentation, *Acta Mater.* 50 (2002) 23–38.
78. K. Hong, K. Kim, S. Kim, I. Lee, H. Cho, S. Yoo, H.W. Choi, N.-Y. Lee, Y.-H. Tak, J.-L. Lee, Optical Properties of WO<sub>3</sub>/Ag/WO<sub>3</sub> Multilayer As Transparent Cathode in Top-Emitting Organic Light Emitting Diodes, *J. Phys. Chem. C* 115 (2011) 3453–3459.

79. P. Boher, P. Houdy, P. Kaikati, L.J. Van Ijzendoorn, Radio frequency sputtering of tungsten/tungsten nitride multilayers on GaAs, *J. Vac. Sci. Technol. A Vacuum, Surfaces, Film.* 8 (1990) 846-850.
80. J.W. Klaus, S.J. Ferro, S.M. George, Atomically controlled growth of tungsten and tungsten nitride using sequential surface reactions, *Appl. Surf. Sci.* 162 (2000) 479–491.

## **Vita**

Oscar Roberto Nunez was born on November 22, 1990 in El Paso, Texas. The first son of Oscar Nunez and Elida Nunez, he graduated with a bachelor's degree in Mechanical Engineering from The University of Texas at El Paso. In order to pursue a master's degree in Mechanical Engineering he stayed at The University of Texas at El Paso. During his master's, he worked as a teaching assistant and research assistant for the Mechanical Engineering department and was a member of the cSETR center. He was also able to publish a scientific article in Thin Solid Films journal that includes results from this work. In fall 2015, he graduated with a Master of Science degree in Mechanical Engineering and proceeded further to pursue his Ph.D. in the ESE program at UTEP.

Permanent address: 10253 Renfrew Dr.

El Paso, Texas, 79925

This thesis/dissertation was typed by Oscar Roberto Nunez.